scientific reports

Check for updates

OPEN

Adsorption of Acid Yellow 36 and direct blue 86 dyes to *Delonix regia* biochar-sulphur

Ahmed Eleryan[1], Uyiosa Osagie Aigbe[2], Kingsley Eghonghon Ukhurebor[3], Mohamed A. Hassaan[1], Safaa Ragab[1], Otolorin Adelaja Osibote[2], Ismail Hossain[4] & Ahmed El Nemr[1]✉

This study aims to investigate a new approach to removing hazardous dyes like Direct Blue 86 (DB86) and Acid Yellow 36 (AY36) from aqueous environments. *Delonix regia* biochar-sulphur (DRB-S), made from *Delonix regia* seed pods (DPSPs), is an inexpensive and environmentally friendly adsorbent. Different characterization investigations using BJH, BET, FTIR, SEM, DSC, TGA, and EDX were utilized in the descriptions of the DRB-S biosorbent. The optimal pH for AY36 dye and DB86 dye adsorption to the DRB-S adsorvbent was at pH 1.5. For the adsorption of AY36 and DB86 to DRB-S, equilibrium was attained at 30 and 90 min of reaction time interaction. The Langmuir model (LGM) and pseudo-second-order-model (PSOM) best describe the biosorption of both dye molecules to the biosorbent owing to the equal and homogeneous spread of the dye molecules over the biosorbent porous surface and a chemisorption process which involved the valency force through the exchange of electrons between the dye molecules and the prepared biosorbent. The determined biosorption capacities for both dyes (AY36 and DB86) were found to be 270.27 mg/g and 36.23 mg/g, respectively. In conclusion, this recently synthesised DRB-S adsorbent exhibited an impressive sorption capacity and successfully removed AY36 and DB86 dyes. This suggests that the biosorbent has potential applications in wastewater treatment and can be recycled without affecting its adsorption effectiveness.

Keywords Adsorption, Biochar, Dye removal, Delonix regia seed pods, Wastewater treatment

Globally, a serious environmental issue is water contamination. Numerous toxins, mostly released during industrial and agricultural processes and some domestic activities, substantially impact water contamination[1–4]. Discharging untreated dye effluents is one of the main causes of water pollution. These dyes are toxic to humans as well as plants and aquatic life. Consequently, one of the most prevalent contaminants in freshwater is dyes, released by various industrial sectors, including textiles, paint, leather, cosmetics, paper, and pulp. Even in deficient concentrations, dyes can aesthetically impact water bodies[5,6]. Non-biodegradable dyes harm terrestrial and atmospheric ecosystems when discharged or used in other ways, harming aquatic ecosystems by lowering the amounts of dissolved oxygen in water bodies[7,8].

According to their chemical structure, especially chromophore moieties responsible for colour, dyes used in textiles are considered into different classess as azo, triphenylmethane, anthraquinone, cyanine, indigoid, xanthene, etc., with azo dyes being one of the largest classes of commercialized synthetic dyes[9–11]. Acid Yellow 36 (AY36) also known as Metanil Yellow is a poisonous azo dye with chemical formula $C_{18}H_{14}N_3NaO_3S$ and molecular weight of 375.4 g/mol. Owing to it being water soluble, it is used leather, paper, beverage and textile industries. According to animal research, it is hepatoxic and neurotoxic. When it comes in contact with the skin, it induces allergic dermatitis and noxious methaemoglobinaemia and cyanosis in humans. It is indicative this dye shows tumour producing effects and may lead to intestinal and enzymic disorder in the body of humans[12]. Direct blue 86 (DB86), also known as Direct Fast Blue GL or Direct Fast Turquoise Blue GL with a chemical formula $C_{32}H_{14}CuN_8Na_2O_6S_2$, is a grey blue to blue powder, well soluble in water and an anionic commercial dye generally applied in paper industries, viscose dyeing and printing, wool and organic pigments manufacturing and cotton printing[13,14]. For colouring fibres such as wool, silk, and other textiles, typical azo dyes like AY36 and

[1]National Institute of Oceanography and Fisheries (NIOF), Kayet Bey, Elanfoushy, Alexandria, Egypt. [2]Department of Mathematics and Physics, Cape Peninsula University of Technology, Cape Town, South Africa. [3]Department of Physics, Edo State University, Uzairue, Edo State, Nigeria. [4]Department of Nuclear and Renewable Energy, Ural Federal University, Yekaterinburg, Russia. ✉email: ahmedmoustafaelnemr@yahoo.com; ahmed.m.elnemr@gmail.com

DB86 are also utilized in the textile sector[15,16]. In addition to being used by the textile industry, AY36 and DB86 dyes have additionally been reported to have been utilized in the production of pigment, shoe polish, laundry detergent, cleaning agents, and soap. However, due to their carcinogenic effects, their utilization in the food industry is strictly banned[15,16]. AY36 and DB86 dyes are colorants for acrylic fibres that are extensively utilized in the printing and textile industries. They may exist at different pH levels in cationic and zwitterionic forms[15,16]. These dyes have various industrial applications, but their runoffs pose a risk to plants, animals, aquatic life, and the ecosystem as a whole[2,16]. Cancer, allergies, and skin disorders are reportedly among the health problems that can arise from individuals drinking and absorbing dye-contaminated water[15,16].

A critical characteristic of the ecological management and sustainable development as industries continues to develop globally and producing huge amount of wastewater containing various pollutants is the treatment of industrial effluent. In response to this challenge, the search for advanced and effective treatment technologies, which is joined with developing trends in process optimization and regulatory compliance is influencing the treatment of industrial effluents. With the growing intricacy and unpredictability of industrial runoffs, there is a rising demand for multipurpose and robust treatment solutions capable of addressing a huge variety of pollutants[17].There have been reports of the effective removal of these dyes from single and binary aqueous solutions using techniques such as adsorption/ biosorption[6], coagulation/flocculation[18], the electro-Fenton process[19–21], catalytic oxidation[22], ultrafiltration[23], ozonation[24–27], biological activation[28], and microbial fuel cells[29], before these synthetic dyes such as AY36 and DB86 from industrial effluents are being released into the environment[15,16].

According to several studies, one of the most often used ways to remove effluents such as metals and dyes from industrial wastes is the biosorption or adsorption of dyes onto activated carbon[4,7,30–37]. The ability of various agricultural wastes, such as tree fern, bark, rice husk, cotton waste, sugarcane dust, and watermelon wastes, as well as other low-cost adsorbents to adsorb dyes and remove various basic and acid dyes, has also been explored[4,7,38–46]. Numerous studies have also documented the removal of dyes from wastewater using biochar made from various biomasses, such as animal waste, plant and algal biomass, residential and forest waste, sewage sludge, etc[47–50]. Using biochar for wastewater treatment is favourable because of its large surface area and high number of surface functional groups (FGs)[47,51–56]. The use of biochar as an adsorbent has several benefits, including being economical, simple to use, and eco-friendly. Various precursors are readily accessible for making biochar, and it has also been reported that biochar has the potential to be recycled and has a better adsorption capacity than other common adsorbents[2,51,56,57].

Therefore, the goal of this study is to investigate a novel approach to the removal of hazardous dyes (AY36 and DB86 dyes) from aqueous environments using *Delonix regia* biochar-sulphur (DRB-S), which was made from *Delonix regia* seed pods (DRSPs). *Delonix regia* is a leguminious plant of the sub-family *Caesalpinoideae*. It is generally grown as an orbnamental or agroforestry tree and produces a huge amount of seed pods and seed during the fruiting season and at present-day are not used. There are not any documented tonnage of seeds produced yearly, possibly due there has not been no reported viable value. The seeds of this plant rots and are wasted owing to that they are put into use[58]. DRB-S is an environmentally acceptable and reasonably priced adsorbent with many surface FGs. To the best of the authors' knowledge, this is the first research to employ DRB-S to remove the dyes AY36 and DB86, which makes it unique. The batch biosorption studies for confiscating AY36 and DB86 dyes from industrial untreated dye effluents were characterized, and the optimization of the various parameters and factors was highlighted. Furthermore, an estimate of the thermodynamics, kinetics, and adsorption isotherms was considered. The basis for this recent study was to establish the use of DRB-S as one of the effective activated biomass-based biosorbents for the removal of AY36 and DB86 dyes utilizing the biosorption technique from industrial untreated dye effluents before being discharged into the nearby water bodies (that will sequentially contaminate the aquatic environment as well as the entire environment), and this will enormously be of great benefit in extenuating environmental contamination from industrial untreated dye effluents and contribute significantly to the desired safety and sustainability of our environment.

Materials and methods

Instrument and materials

DPSPs were collected from a local area in Alexandrian and utilised as the raw material to create DRB-S, an adsorbent substance. Sulfuric acid (H_2SO_4, Purity 98%), AY36 and DB86 dyes were obtained from Sigma Aldrich, USA. Concentrations were measured using an analytical Jena digital spectrophotometer (SPEKOL1300 UV/Visible spectrophotometer) in conjunction with 1 cm optical path glass cells, a shaker (JSOS-500) for mixing procedures, and a pH metre (JENCO 6173) for pH surveys. The adsorption-desorption isotherm of DRB-S was measured in the N_2 environment. Using an instrument (BELSORP – Mini II, BEL Japan, Inc.), the surface area, pore size and pore distribution of DRB-S were determined[59,60]. Monolayer volume (V_m) (cm^3 (STP), surface area (S_{BET}) (m^2/g), average pore diameter (MPD) (nm), total pore volume (p_0/p_0) (cm^3/g) and energy constant (C) values of DRB-S were obtained by modeling of the adsorption-desorption graph. The microporous surface area (S_{mi}), mesoporous surface area (S_{mes}), mesoporous volume (V_{mes}), and microporous volume (V_{mi}) of DRB-S were calculated by the Barrett–Joyner–Halenda (BJH) model. The calculations were carried out using the BELSORP analysis software. Using the BJH approach, the pore size dispersion was also ascertained from the desorption isotherm[61]. An investigation of the form of the biochar surface was conducted using a scanning electron microscope (SEM; QUALITY 250). Fourier Transform Infrared (FTIR) spectroscopy (VERTEX70) and the ATR unit model V-100 were used to investigate the FGs on the surface of DRB-S. IR-observable FGs on the DRB-S surface were identified in the 400–4000 cm^{-1} wavenumber region using FTIR spectroscopy in combination with the platinum ATR unit. Employing the SDT650-Simultaneous Thermal Analyzer apparatus, thermal analyses were conducted at a ramping temperature of 10 °C/min throughout a temperature range of 50–1000 °C.

DRB-S preparation

DPSPs were extensively cleansed with tap water many times to remove any dust, and they were thereafter dried in a furnace at 115 °C for twenty-four hours before being ground and pulverised. A total of 120 g of powdered DPSPs was heated at 260 °C in 600 mL of 85% H_2SO_4 solution for 6 h, then diluted with distilled water, filtered and then washed with distilled water until pH 7. The DRB-S was then cleaned with EtOH and dried at 115 °C in a furnace. Biochar with the designation DRB-S was produced as a consequence of this reaction.

Batch adsorption experiment

A batch adsorption experiment was used to assess the sorption capacity, thermodynamic, and kinetic properties of DRB-S. A series of 300 mL Erlenmeyer flasks were filled with 100 mL of AY36 (Metanil Yellow, $C_{18}H_{14}N_3NaO_3S$) and DB86 (Solvent Blue 38, $C_{32}H_{14}O_6N_8S_2CuNa_2$) dyes (Fig. 1) solutions at various starting concentrations and DRB-S at various weights were shaken for a predetermined amount of time at 200 rpm. Solution pHs were raised or lowered to the appropriate levels with 0.1 M NaOH or HCl. Furthermore, during the adsorption equilibrium investigations, the pH of the solution was maintained at the intended level. Taking a sample (0.1 mL) from the solution at regular intervals (removed from the adsorbent) allowed for the determination of the AY36 and DB86 dye concentration using a spectrophotometer set at $\lambda_{max} = 594$ and 615 nm, respectively. All experiments were repeated three times with a difference of less than 2.5%, and only the average values were used in the calculations. The q_t of DRB-S was calculated using Eq. (1).

$$q_t = \frac{(C_0 - C_t)}{W} V \tag{1}$$

where C_0 (mg/L) is the AY36 and DB86 dyes initial concentration; C_t (mg/L) is the remaining AY36 and DB86 dyes concentration at the end of time t; q_t (mg/g) is the adsorption capacity of DRB-S at time t; W (g) is the mass of the DRB-S and V (L) is the volume of the AY36 and DB86 dyes solutions.

To examine the impact of pH on the adsorption of AY36 dye and DB86 dye ions by DRB-S, studies were achieved at different pH values (1.11 to 13.15) and (1.56 to 13.32), respectively, by adding 0.1 g DRB-S to 100 mL of solutions containing 100 ppm of AY36 dye and 50 ppm of DB86. The mixtures were agitated for 150 min at 200 rpm when the mixtures were at room temperature.

AY36 dye and DB86 dye solutions with varying initial concentrations (50–150 ppm) were made, and isotherm measurements and the effect of DRB-S dose on the adsorption of AY36 dye and DB86 dye ions were investigated. Intervals between 0.75 and 1.75 g/L of DRB-S doses and AY36 dye and DB86 dye solutions with diverse starting concentrations were used to measure the AY36 dye and DB86 dye concentrations. The mixtures were agitated at 200 rpm and 25 °C. Every adsorption investigation was carried out in triplicate, and the results are presented as an average.

Results and discussion
DRB-S characterization

Using FT-IR spectroscopy, the FGs present on the surface of the resulting DRB-S adsorbent were identified. The FTIR graph of the raw DPSPs and the FTIR graph of the DRB-S were compared, as shown in Fig. 2a, b. The FT-IR spectra of the materials show changes in their FGs. The stretching oscillation of the O-H present in the DPSPs and DRB-S is demonstrated by the band between 3583.25 and 3348.50 cm⁻¹ (Fig. 2). The presence of –CH_2 stretching groups in DPSPs is suggested by the high absorption peaks between 2925.89 cm⁻¹ (Fig. 2a). These groups were enlarged in DRB–S and appeared at 2920.09 cm⁻¹ (Fig. 2b). The C=O stretching of the ester groups in the DPSPs is responsible for the high absorption band at 1733.76 cm⁻¹ (Fig. 2a). This band was later transformed into a carboxyl group in DRB-S at 1704.71 cm⁻¹ (Fig. 2b). Nevertheless, the strength at 1704.71 cm⁻¹ increased when DRB-S was compared to raw DPSPs, indicating that sulphuric acid treatment may increase the carbonyl (C=O) group. The bands at 1631.76 cm⁻¹ suggest that the β-ketone's C=O stretching oscillation was nearly existent in the DPSPs. This oscillation shifted to 1603.56 cm⁻¹ in DRB-S with high intensity, and it might also be a stretching vibration of –C=C– in DRB-S (Fig. 2b). The DPSPs' C-O FG is shown by the peaks at 1513.67–1252.28 cm⁻¹. This group was replaced by the band at 1399.72 and 1367.29 cm⁻¹ in DRB–S, which displayed the sulfonyl group
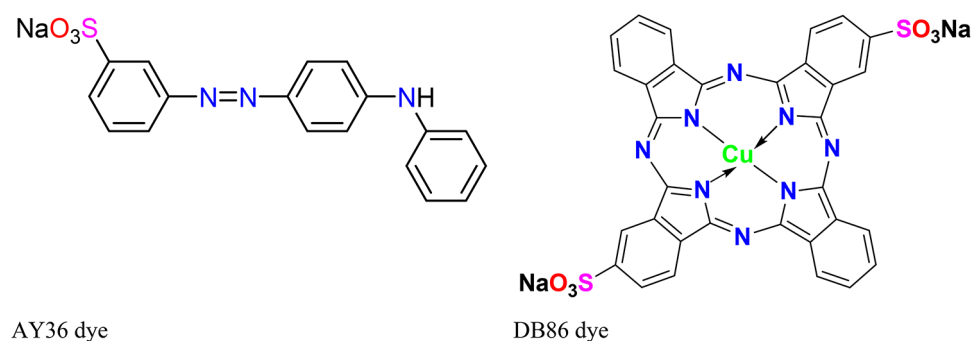

AY36 dye   DB86 dye

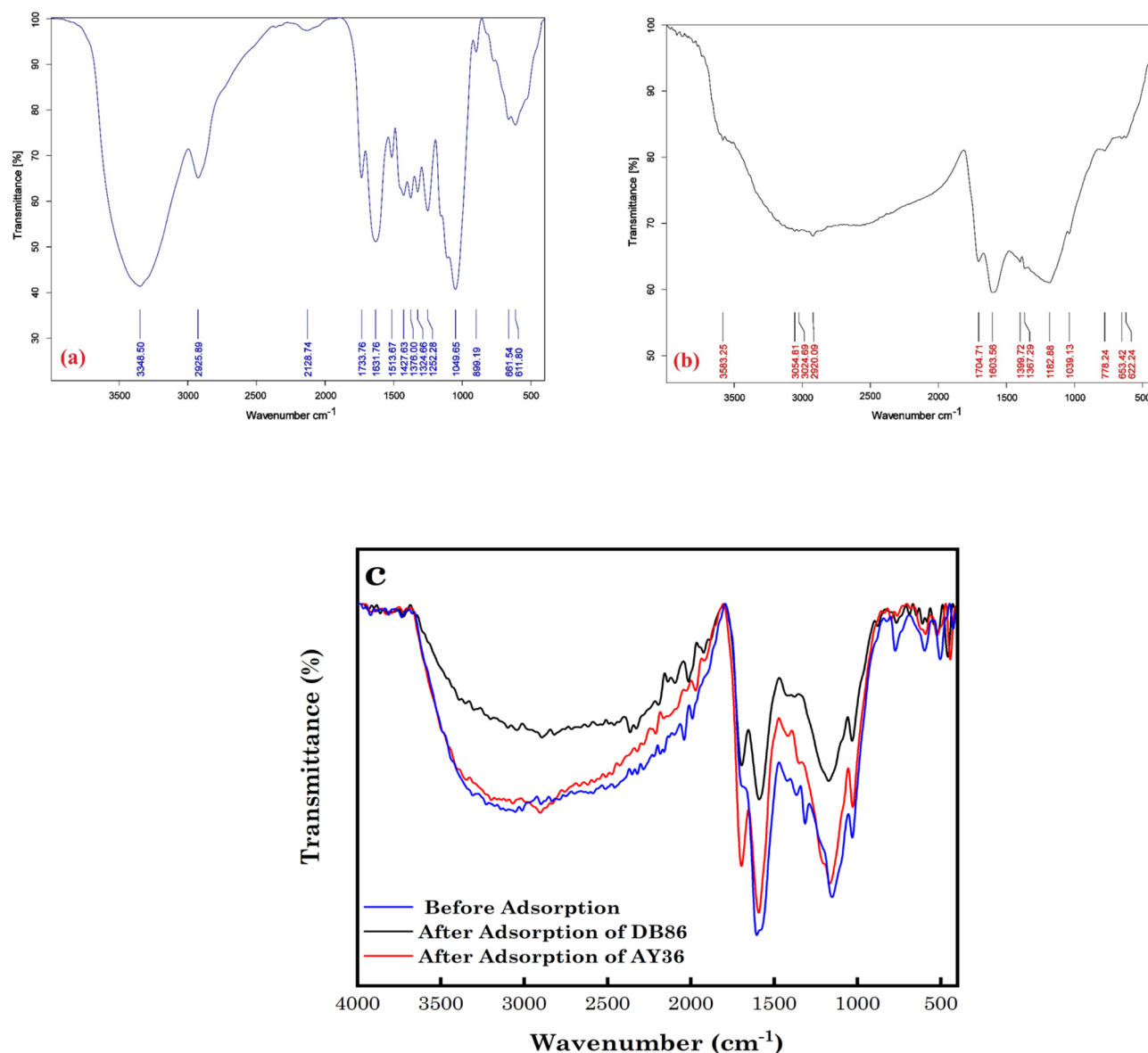**Fig. 1.** Structure of AY36 and DB86 dyes.

Fig. 2. FTIR graphs of (a) DPSPs, (b) DRB-S and (c) before and after adsorption of AY36 and DB86 dyes to DRB-S.

(S=O) stretching vibration (Fig. 2b). Additionally, the development of peaks at 1182.88 and 1039.13 cm^{-1} was facilitated by the dehydration process with H_2SO_4. These peaks resulted from the production of $-SO_3H$ and S=O groups in DRB-S. These bands show that the DPSP treatment with H_2SO_4 results in the creation of the DRB-S. The DPSPs showed a more noticeable rise in the $-C-O-C-$ asymmetric stretching FG at 1049.65 cm^{-1} (Fig. 2a), compared to DRB-S, which showed a partly weaker increase[54–57]. As observed in Fig. 2c, there was a red shift in most of the peaks of $-C=C-$, $-SO_3H$, O–H and S=O after the adsorption of AY36 and DB86 to DRB-S with associated intensity changes. This indicates that the uptake of the dye molecules was attributed to these FGs.

To find out how H_2SO_4 affected the DRB-S's surface characteristics, the N_2 adsorption-desorption isotherm of the DRB-S was studied. The BET and BJH methods were used to compute the specific surface and mesopore areas, respectively. Figure 3 shows the textural properties of DRB-S, including BET-specific surface area, mass of mesopores, mesopore area, total volume of pores, mesopore distribution peak, average pore diameter, and monolayer volume. The DRB-S has a relatively tiny BET-specific surface area of 14.745 m^2/g. DRB-S had a monolayer volume value of 3.3878 cm^3 (STP) g^{-1}. DRB-S has a total volume value of 1.8975×10^{-2} cm^3/g. DRB-S had mean pore diameters of 5.1474 nm. The values of 14.923 m^2/g, 2.1973×10^{-2} cm^3/g, and 1.22 nm were found to be the mesopore volume, meso surface area, and mesopore distribution peak values of DRB-S, respectively.

The DRB-S is shown in SEM pictures in Fig. 4a, where it is clear that it is clean and impurities-free. The DPSPs' pore structure remained unharmed by the intense sulfuric acid treatment. The particle pore size distribution shows that the particle pore sizes were within the range of 4072–17,200 nm, and the determined average particle pore size distribution of the DPKB-S was 9821 ± 1.65 nm according to ImageJ assessment (Fig. 4b).
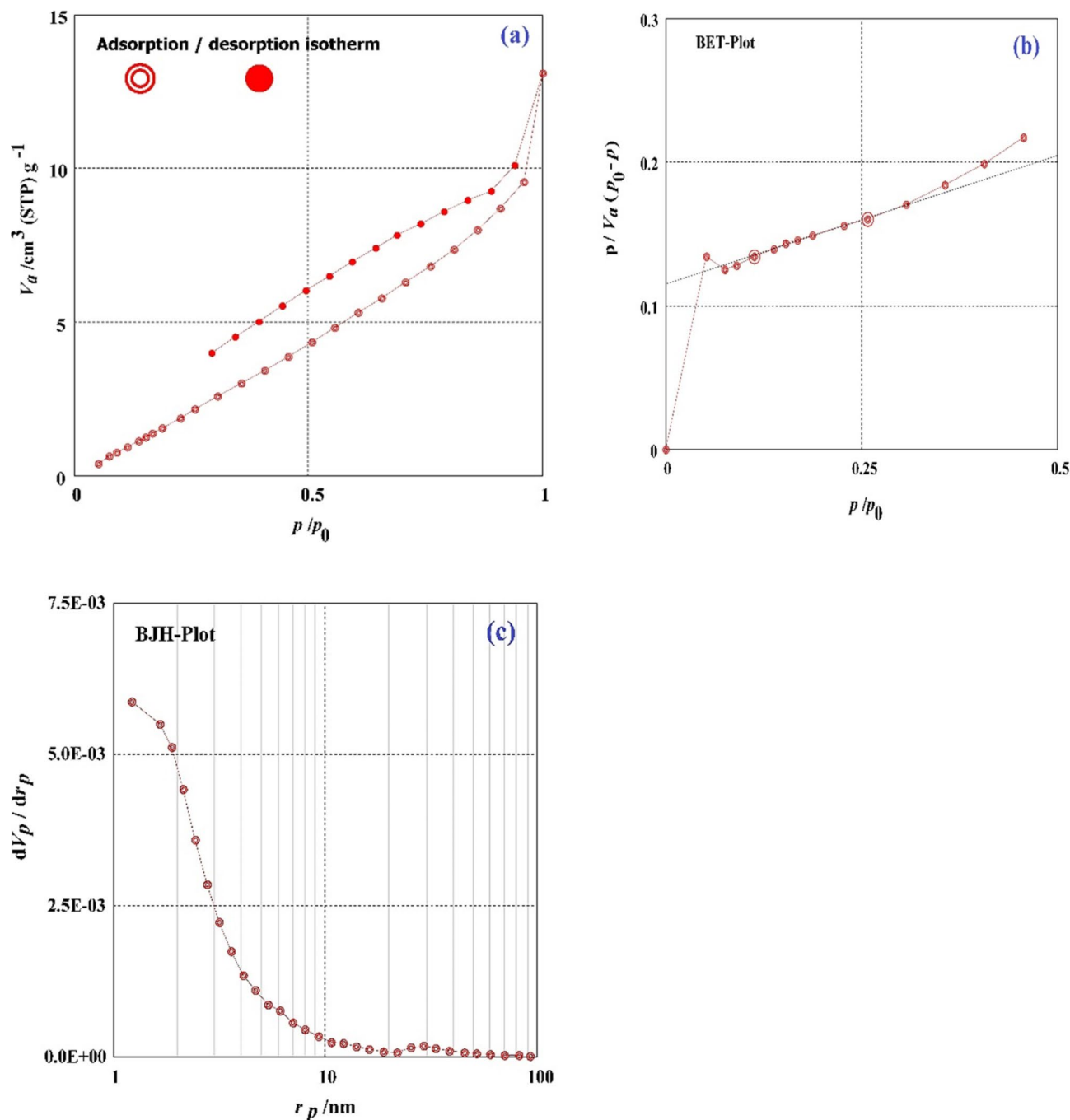
Fig. 3. (a) Graph of N_2 Adsorption-Desorption, (b) Graph of the BET, (c) Graph of the BJH of the DRB-S.

The DRB-S adsorbent chemical composition was studied using scattered X-ray spectrometry (EDX). The percent of each element is presented in Table 1, which indicates that, in addition to carbon mass %, which makes up 56.26% of the sample, there are around 41.50 and 0.37% of oxygen and sulphur, respectively.

The impact of structural variations on the operating temperature and degradation behaviour of the DRB-S samples and raw date palm kernel was assessed using thermal gravimetric analysis (TGA). Every sample was heated from 50 to 1000 °C in a N_2 atmosphere. Figure 5 displays the TGA, Differential Thermal Analysis (DTA) and Differential Scanning Calorimetry (DSC) analytical curves for DPSPs and DRB-S. The first weight reduction was caused by the evaporation of water in the raw DPSPs and DRB-S, and it peaked before 150 °C. Raw DPSPs and DRB-S lost weight as a result of the breakdown of many acidic oxygen FGs that occurred as the temperature rose beyond 150 °C. Moreover, acidic groups break down at different temperatures. For example, phenol breaks down at a greater temperature than lactones, anhydrides, and carboxylic groups. Raw DPSPs exhibit a high weight loss at temperatures up to 328.5 °C and the final weight loss occurs between 328 and 450 °C. DRB-S shows three weight losses at temperatures between 25 and 150, 150–380 and 380–950 °C, which explains the
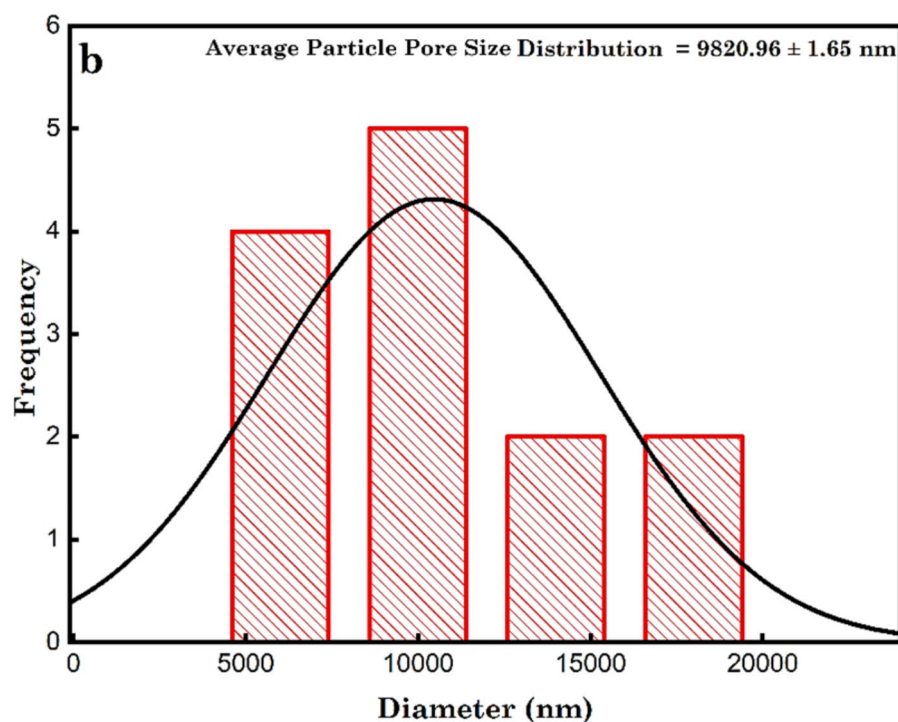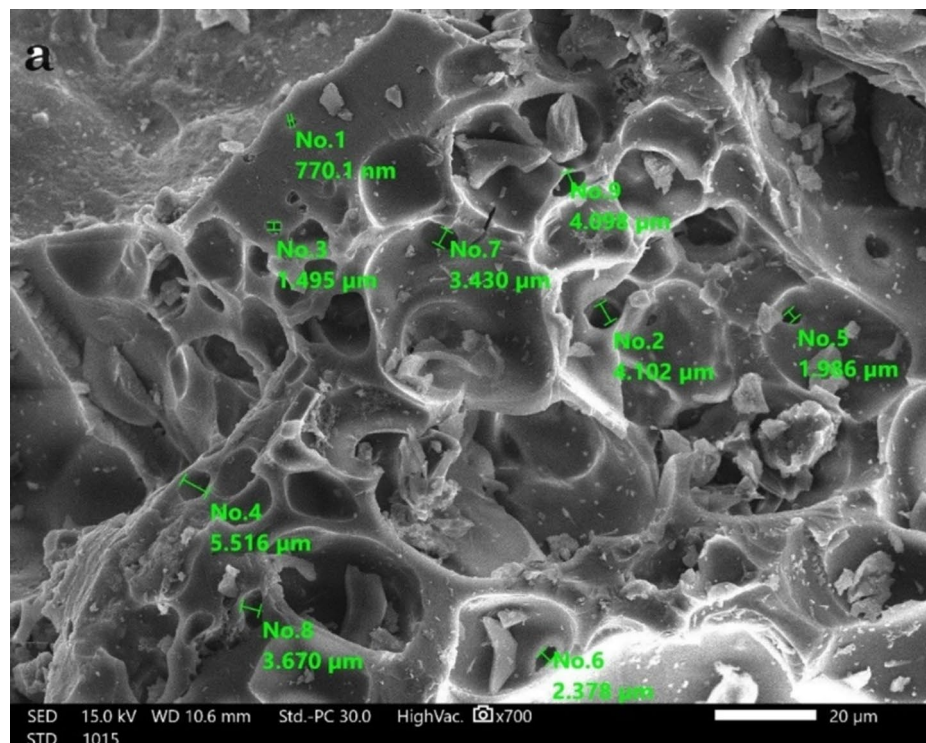
Fig. 4. (a) SEM image of DRB-S using High vacuum SEM at magnification ×700 and 15.0 kV, and (b) particle pore size distribution of DRB-S.

higher stability of DRB-S compared to the raw DPSPs. TGA curve of DRB-S converged at temperatures > 400 °C due to carbon breakdown in biomass. At the finishing temperature, various weight loss percentages of 78.03 and 48.06% were obtained for raw DPSPs and DRB-S, respectively, indicating the greater stability of DRB-S.

The DTA graph of DRB-S and raw DPSPs is illustrated in Fig. 5a. The DTA curve of the raw DPSPs (blue) peaked at two points at temperature (T_p 58.10 and 328.30 °C), while the curve of DRB-S (blue) peaked at three points at temperature (T_p 85.40, 350.06 and 454.66 °C) (Fig. 5a). As can be seen from the DTA curve to produce

	DRB-S	
Elements	Mass%	Atom%
C	56.26 ± 0.33	63.61 ± 0.37
O	41.50 ± 0.67	35.22 ± 0.57
S	0.37 ± 0.04	0.16 ± 0.02
Na	1.53 ± 0.10	0.90 ± 0.06
Ca	0.34 ± 0.04	0.12 ± 0.01
Total	100.00	100.00

Table 1. EDX results of prepared DRB-S.

DRB-S adsorbents from raw DPSPs, dehydration of raw DPSPs (blue) showed two well-resolved degradation bands. The degradation bands of raw DPSPs (blue) decreased from three to two at higher temperatures after treatment with 85% H_2SO_4, demonstrating that the degree of degradation was strongly affected by H_2SO_4 treatment.

DSC may be used to compare materials based on thermal transitions. Figure 5b depicts the DSC graph of DRB-S (red) and raw DPSPs (blue). The crystallisation temperatures (T_C) of DPSPs are 72.76 °C, while DRB-S displays T_C values of 82.11 °C. When the temperature rises, DRB-S melts at 587.95 °C, while DPSPs melts at 565.13 °C. A lower T_m was shown by DPSPs, whereas the highest T_m was shown by DRB-S. The grains became more crystalline due to the higher transitional temperatures, improving their structural stability and resistance to gelatin disintegration. Based on Fig. 6b, a weight loss was observed in the TGA analysis of before and after adsorption of AY36 and DB86 dye molecules to DRB-S at 150, 328, 450, and 950 °C. At 150 and 950 °C, it was observed that the DRB-S sorbent had a greater weight loss of 14.56% and 47.67% (Fig. 6b). After the adsorption of AY36 and DB86 dyes to DRB-S, there was a decrease in weight loss of 12.75% and 10.92% noticed at 150 °C. At 950 °C, there was also a reduced weight loss of 46.83% and 42.69% observed after the adsorption of AY36 and DB86 dyes to DRB-S (Fig. 6c, d). These reduced weight loss after adsorption of AY36 and DB86 dyes at 150 and 950 °C were ascribed to the decomposition of the dye molecules.

The DRB-S XRD is shown in Fig. 7 and shows an amorphous carbon structure with arbitrarily oriented aromatic sheets. A tiny and broad peaks located at $2\Theta = 44.6°$ and $21.7°$ which were indexed at 101 and 002 planes of amorphous carbon or common feature of a non-crystallite structure of activated carbon as well as bear a resemblance to the graphitic hexagonal structure of carbon based materials[66–69]. The average crystallite size (D_{hkl}) of the miniscule powdered particles in the hkl direction was obtained using the Debye Scherrer equation (Eq. 2).

$$D_{hkl} = \frac{K\lambda}{\beta_{hkl} \cos(\theta_{hkl})} \tag{2}$$

Where h, k, l, K, λ, θ and β represent the miller indices, the shape factor (0.9), the wavelength of the diffraction beam (0.15406 nm), Bragg angle and the full width half medium (FWHM) of the X-ray diffraction peaks (radians)[70,71]. The crystalline size of the 002 and 101 peaks were dteremined to be 0.34 and 0.50 nm.

Equations 3–7 show the average crystallite lattice parameters of carbon material (interplanar spacing of the aromatic layers of D_{002} and D_{100}), crystallite height of the plane 002 (L_c), crystallite diameter of the plane 101 (L_a) and the average number of effective aromatic layer per carbon crystallite (N_{ave}) were obtained employing the Bragg's equation and the empirical equations obtained from Scherrer equation.

$$D_{002} = \frac{\lambda}{2\sin\theta_{002}} \tag{3}$$

$$D_{101} = \frac{\lambda}{2\sin\theta_{101}} \tag{4}$$

$$L_c = \frac{K_c\lambda}{\beta_{002}\cos\theta_{002}} \tag{5}$$

$$L_a = \frac{K_a\lambda}{\beta_{101}\cos\theta_{101}} \tag{6}$$

$$N_{ave} = \frac{L_c}{D_{002}} + 1 \tag{7}$$

θ_{002}, θ_{101}, β_{002}, β_{101}, K_c and K_a are the X-ray diffraction peaks at 002 and 101, FWHM of the 002 and 101 peaks and K shaped factor constants for 002 (0.89) and 101 (1.84) peaks[72,73]. In Table, the determined D_{002} and D_{101} values were 0.410 (samples have a lower-level ordered crystalline unit relative to hite) and 0.203 nm. While the determined L_c and L_a values were 0.338 and 1.022 nm. The extensive diffraction at 002 peak noticed for DRB-S suggested that the material was extremely disordered, moderately crystallized and tically graphite in phase morphology. Hence this peak is assigned to the graphitic planes. The interplanar spacing f the 002 peak was large to the value of 0.335 nm projected for ideal graphite (JCPDS 00-056-0159). Hence the D_{002} value of
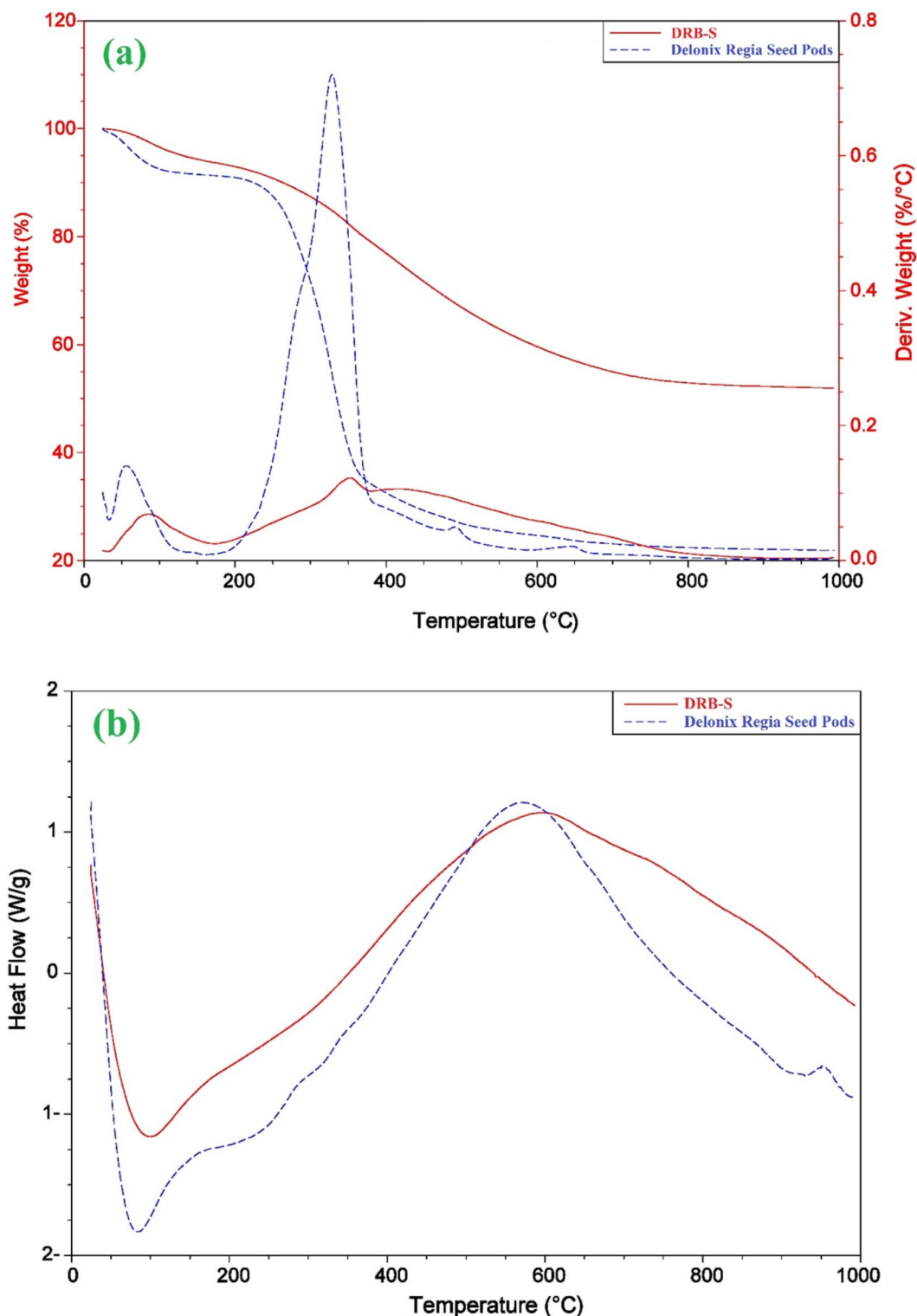
Fig. 5. Graphs of (a) DTA and TGA, and (b) DSC of the DPSPs and DRB-S.

0.410 nm was anticipated to be an effective electrode materials for storage applications. It was also observed that the determined L_a value was larger than the obtained L_c value from peaks 101 and 002. This was suggestive of the growth of the graphitic structure being on the planes[74–76].

pH effect

A critical parameter that controls the sorption of dye to biosorbents is the pH effect (Fig. 8). Dyes are known to occur in an ionic form in a water-soluble solution and the degree of sorption on the surface of the biosorbent is
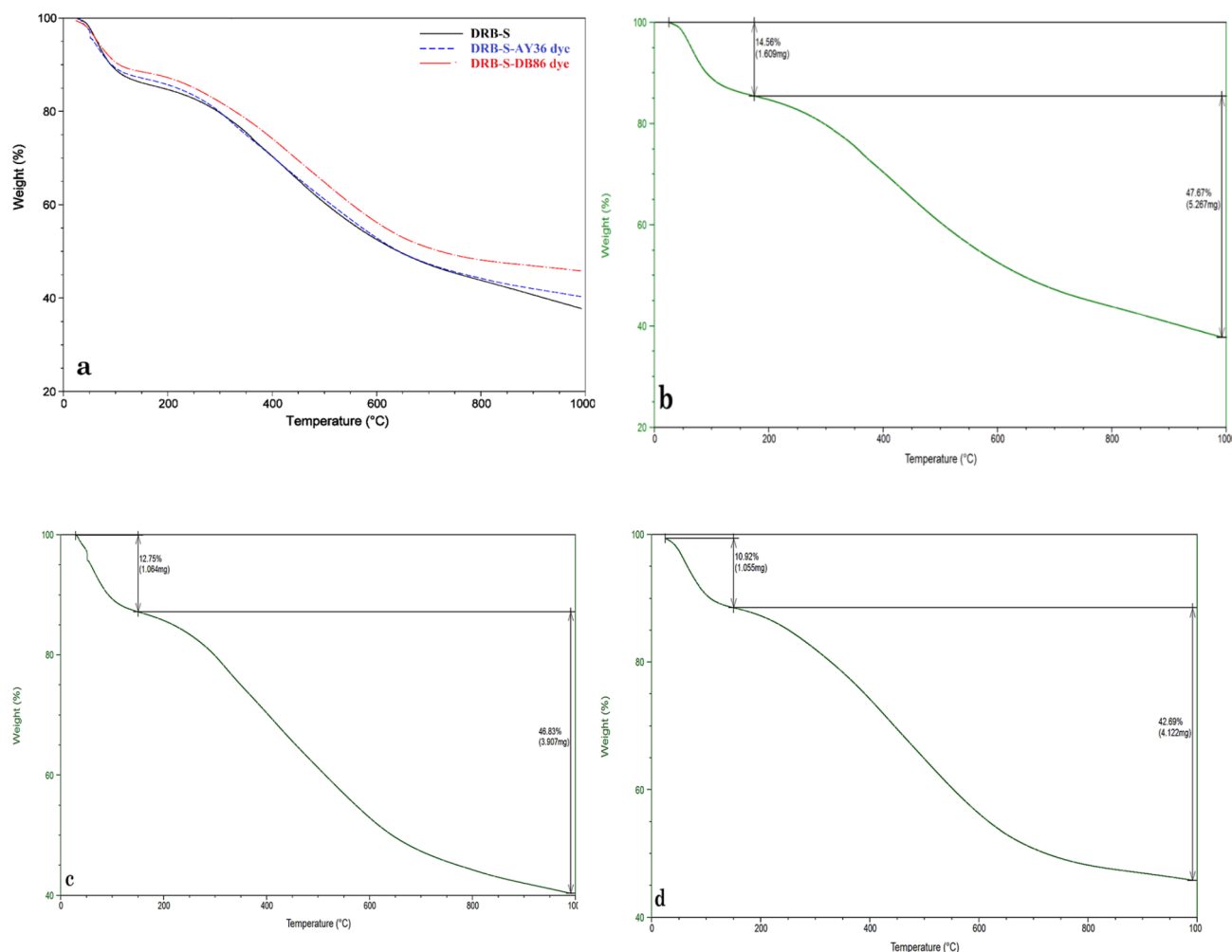
Fig. 6. TGA of (a) DRB-S, before and after of AY36 and DB86 dyes (b) DRB-S, (c) DRB-S-AY36 and (d) DRB-S-DB86 dyes after adsorption.

D$_{002}$ (nm)	D$_{101}$ (nm)	L$_c$ (nm)	L$_a$ (nm)	N$_{ave}$
0.410	0.203	0.338	1.022	1.989

Table 2. Determined interlayer spacing anf Microcrystallite dimesions of DRB-S.

impacted by the biosorbent surface charge, which in turn impacts the pH of the aqueous solution[77,78]. Also, the electrostatic interaction between the biosorbent surface and the dye molecules is enhanced by the variation of the point of zero charge (pH$_{PZC}$) of the biosorbent through the surface variation. The biosorbent surface sites show a positive and negative charge when $pH < pH_{pzc}$ and $pH > pH_{pzc}$[79]. The pH$_{PZC}$ of the prepared biochar was determined to be 12.4 (Fig. 1a). Figure 1b and c show the percentage (%) removal of AY36 (94%) and DB86 (21%) dyes confiscated to the biochar as the pH was varied (pH 1.1–13.2). As observed in Fig. 1b and c, the % removal of AY36 and DB86 dyes sorbed to the biochar decreased with increasing pH, with the optimum % removal of both dyes noticed at pH 1.1. For AY36, this phenomenon was ascribed to the electrostatic attraction between the increased positively charged sites on the biochar surface (hydrogen ions - H$^+$), and the cationic dye molecules. With further increase in the solution pH (basic condition), the surface charged sites on the biochar became negatively charged (hydroxyl ion-OH$^-$) and this led to the electrostatic repulsion between the cationic dye molecules and the negatively charged surface sites on the biochar (excess OH$^-$). A similar trend was observed in the studies of El-Nemr et al.[80], Garg et al.[81] and Thirunavukkarasu et al.[82].

Dosage effect

A critical factor that should be considered and which influences the extent of biosorption of dye is the biosorbent dosage[83]. The % of AY36 dye and DB86 dye confiscated to the prepared biochar (Fig. 9a–f) was observed to increase significantly as the biosorbent dosage and time were improved from 0.75 to 1.75 g/L and 10–150 min for
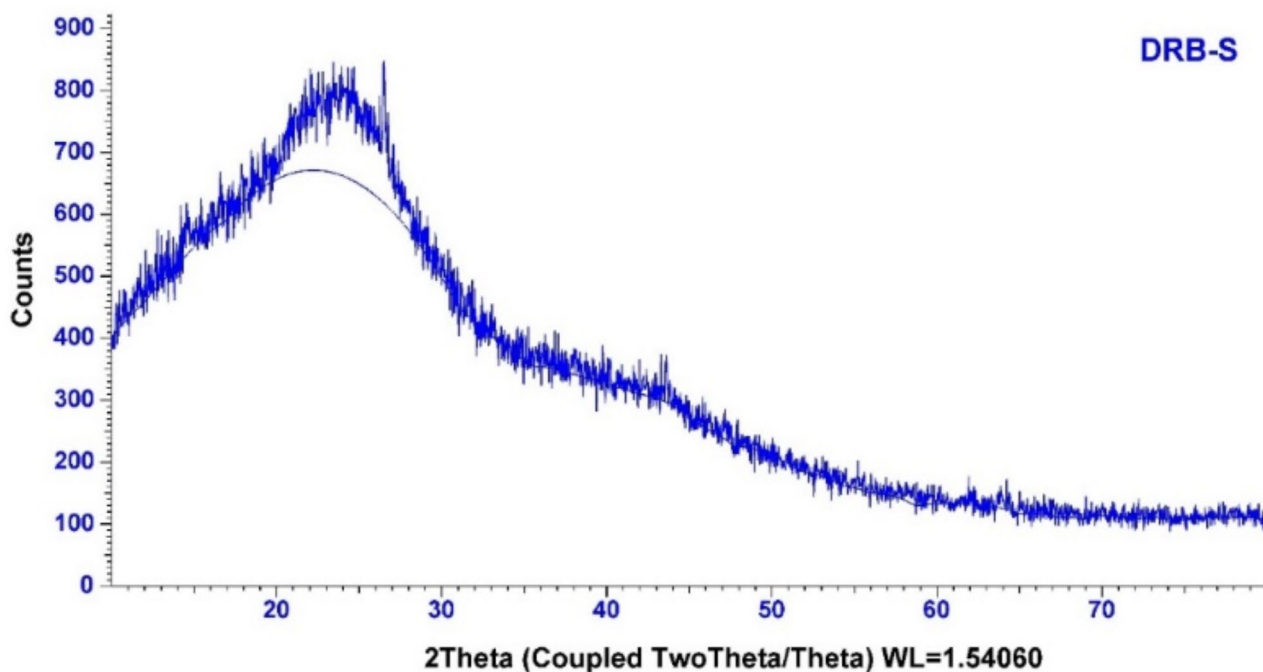
Fig. 7. XRD graph of fabricated DRB-S biochar.

50–100 ppm of both dyes (Tables S1–S4). This occurrence was ascribed to the intensification of the number of available active sites on the biochar surface as the biochar dosage was increased, thereby increasing the % of dye molecules confiscated to the prepared DRB-S[84,85]. As shown in Tables S1–S4, the adsorption capacity was raised by raising the initial dye concentrations and lowered by increasing the dose of DRB-S.

Initial concentration effect

The initial sorbate concentration describes the sorbate molecules partitioning behaviour among the solid biosorbent and the mass liquid solution at equilibrium[86]. The impact of the starting dye concentrations (50–150 ppm) on the biochar's confiscation efficiency is depicted in Fig. 10a–d. As reaction interaction time was increased from 0 to 150 min, it was shown that the optimal removal of AY36 and DB86 dyes decreased with an increase in the starting dye concentrations (Tables S1, S2). It was also noticed that the % of AY36 and DB86 dyes removed was gradually reduced and equilibrium was attained at 30 and 90 min of reaction interaction, owing to the saturation of available accessible active sites on the biochar surface at elevated dye concentrations. At low concentrations, the ratio of the available, accessible active sites on the surface of the biochar was high, hence leading to the increased diffusion of dye molecules from the solution to the active sites of the biochar. This boosted the driving force of the concentration gradient[87–89].

Kinetic models

Kinetic research defines the reaction rates that assess the contact time needed to accomplish the biosorption equilibrium. It is a crucial variable in every biosorption investigation. The rate and mechanism by which the contaminant is removed must be understood very precisely, and for this, the kinetic models explored in this study were the pseudo-first-order model (PFOM), pseudo-second-order-model (PSOM) and the intra-particle diffusion model (IDM) and film diffusion model (FIM)[90]. The linearized form of these different models is given by Eqs. (8)–(11).

$$\log q_e - q_t = \log q_e - K_1 t \tag{8}$$

$$\frac{t}{q_t} = \frac{1}{K_2 q_e^2} + \frac{t}{q_e} \tag{9}$$

$$q_t = K_{IDM} t^{0.5} + C \tag{10}$$

$$\ln(1 - F) = -K_{FD} \times t \tag{11}$$

K_1, K_2 and K_{IDM} are the PFO rate constant (min^{-1}), PSO rate constant (g.mg^{-1}.min^{-1}), ID rate constant (mg. g^{-1}.min$^{1/2}$), and the C is the intersection of the line with the ordinate axis. The value of C gives an idea about the boundary layer thickness. Meanwhile, F and KFD signify fractional attainment of equilibrium and film diffusion rate coefficient (L/min). A plot of ln (1-F) against t, with a zero intercept, indicates that thadsorption procedure is controlled by the diffusion of the liquid film around the adsorbent[91–93]. The plots of the linearized form of
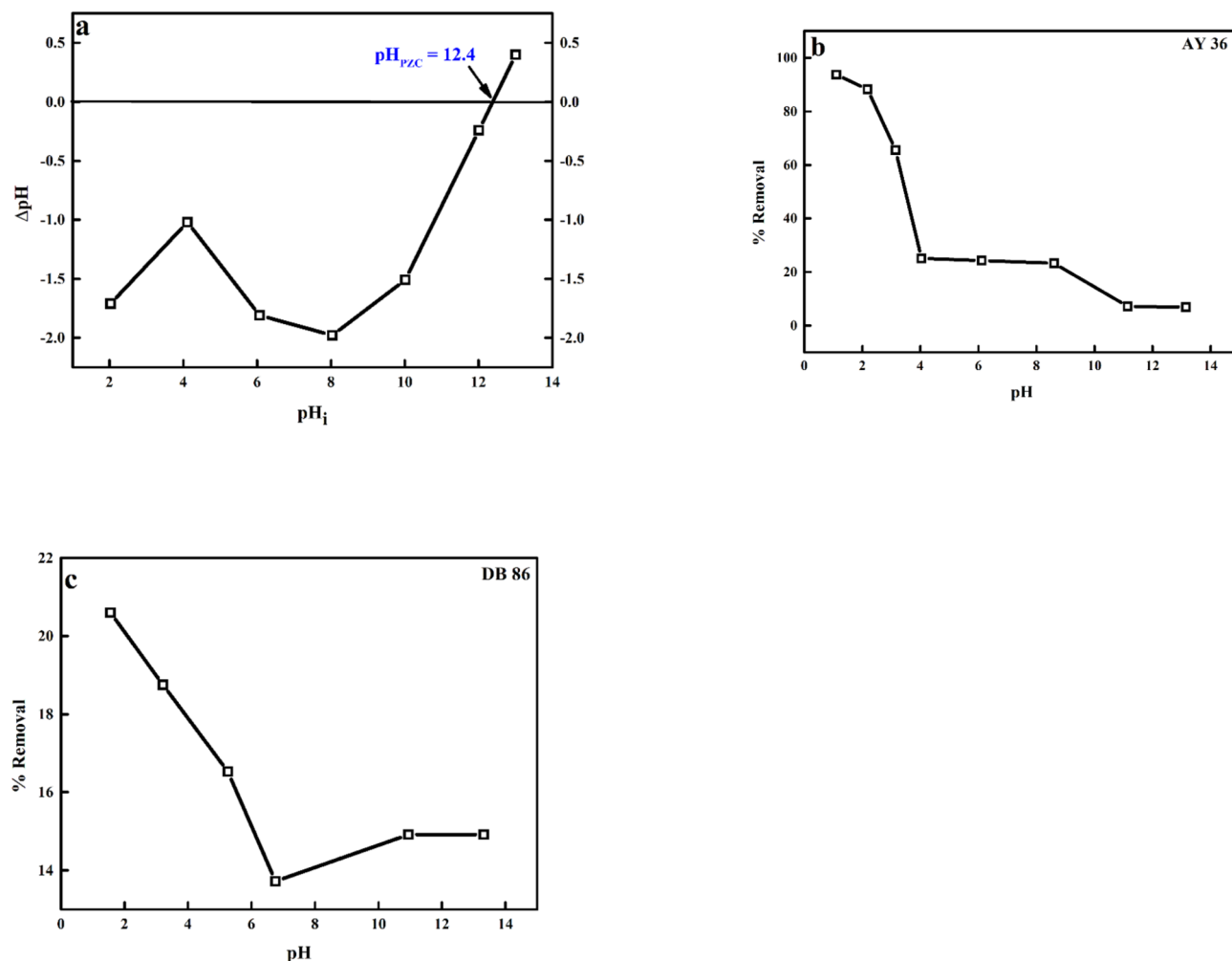
Fig. 8. (a) pH_{PZC} of the prepared biochar-S (DRB-S), (b) pH impact on the biosorption of AY36 dye and (c) DB86 dye onto DRB-S at room temperature.

all models are given in Fig. 11. According to the result provided in Tables 3 and 4, the PSOM best defines the biosorption of AY36 and DB86 dyes to the nanomaterial based on the determined correlation coefficients (R^2) of this model ($> 0.99 -$ close to unity), which was higher than the PFOM. Also, the experimental q_e values of this model were close to the calculated q_e values. From the calculated parameters of IDM and FIM in Tables 5 and 6, the IDM and FIM plots did not offer a straight line that goes through the origin of the plots, and the R^2 values were less than those of the PSOM. This indicated that the diffusion of dye molecules in the liquid film around the prepared biosorbent was not rate-defining steps and diffusion but might advance the adsorption process at the jolt of the biosorption process. Hence, the biosorption process of both dyes to the biosorbent assumed a chemisorption process which involved the valency force through the exchange of electrons between the dye molecules and the prepared biosorbent[94].

Isotherm models
The sorption isotherm defines the association between the biosorbent and the measure of analytic substance in the solution. To explain the mechanism of AB 36 and DB86 dyes biosorption to the biochar, the Langmuir model (LGM) and Freundlich (FDM) model were fitted to the experimental data[95–97].

The LGM assumes that on a homogeneous biosorbent surface, monolayer sorption can take place with no interaction between the sorbates. The linear form of this model is defined by Eq. (12).

$$\frac{C_e}{q_e} = \left(\frac{1}{q_m}\right) C_e + \frac{1}{q_m K_L} \tag{12}$$

q_m, q_e, C_e and K_L signify the optimum biosorption capacity (mg/g), biosorption capacity at equilibrium (mg/g), sorbate concentration in the solution at equilibrium (mg/L) and the LGM constant (L/mg). The sorption effect of the biosorption process can be described by the equilibrium constant R_L of the LGM[98].
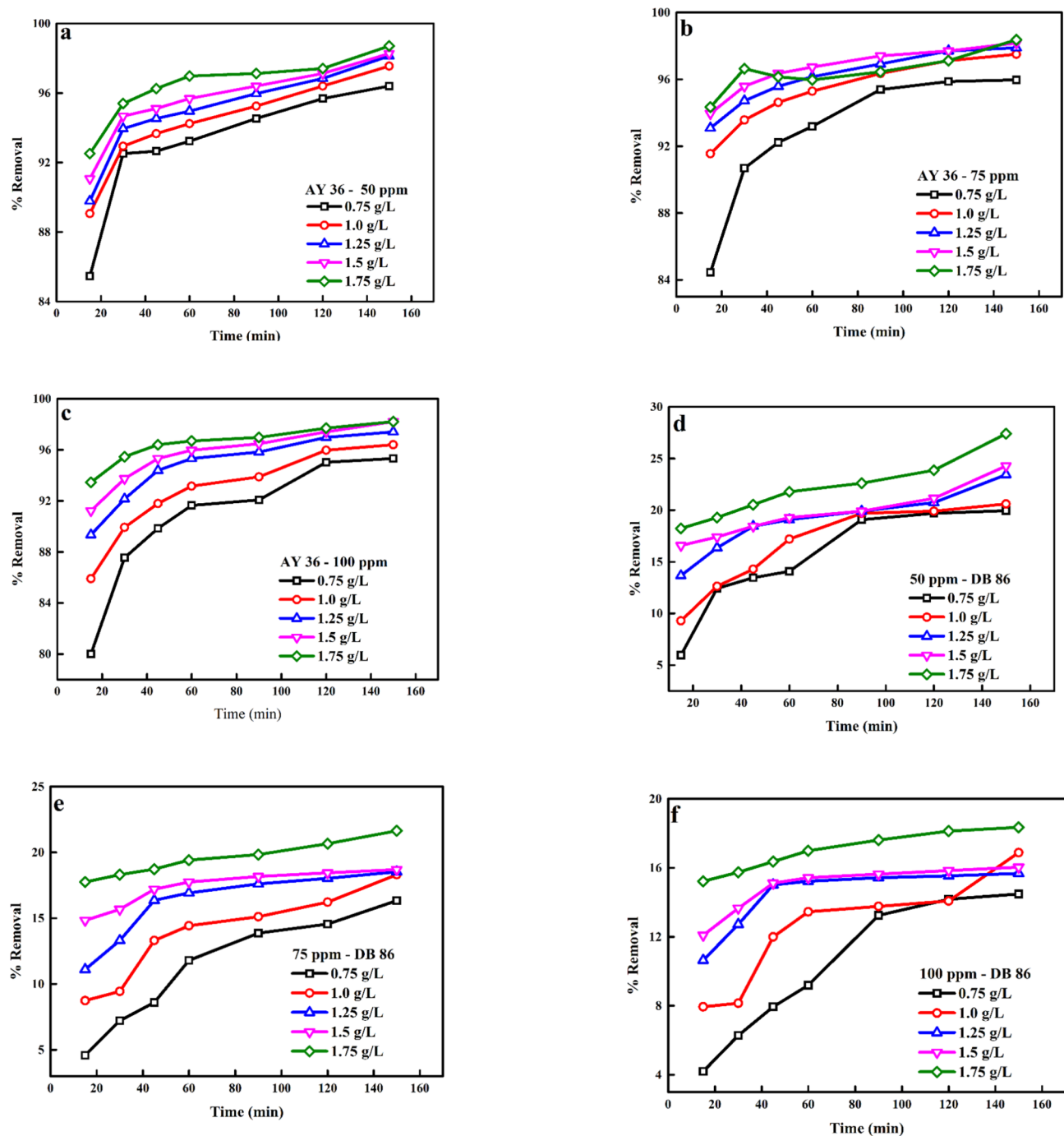
Fig. 9. Effect of biosorbent dosage on the confiscation of (a) AY36 dye—50 ppm, (b) AY36 dye—75 ppm, (c) AY36 dye—100 ppm, (d) DB86 dye—50 ppm, (e) DB86 dye—75 ppm and (f) DB86 dye—100 ppm.

An experimental calculation that is based on the theory that the sorption procedure happens at diverse surfaces having various accessible binding sites with irregular adsorption energies is the FDM. Hence, this model shows that the sorption sites with extreme affinity are filled first. The linear form of this model is given by Eq. (13)[99,100].

$$\log q_e = \log K_F + \frac{1}{n} \log C_e \tag{13}$$

K_F and $1/n$ represent the FDM parameters related to the biosorption capacity and intensity. A favourable biosorption corresponds to a value of $1 < n < 10$[101,102].

The Redlich-Peterson isotherm model (RPM) is a blend of the LGM and FDM. The numerator is the LGM and has the advantage of approaching the Henry region at unlimited dilution. This model is an experimental
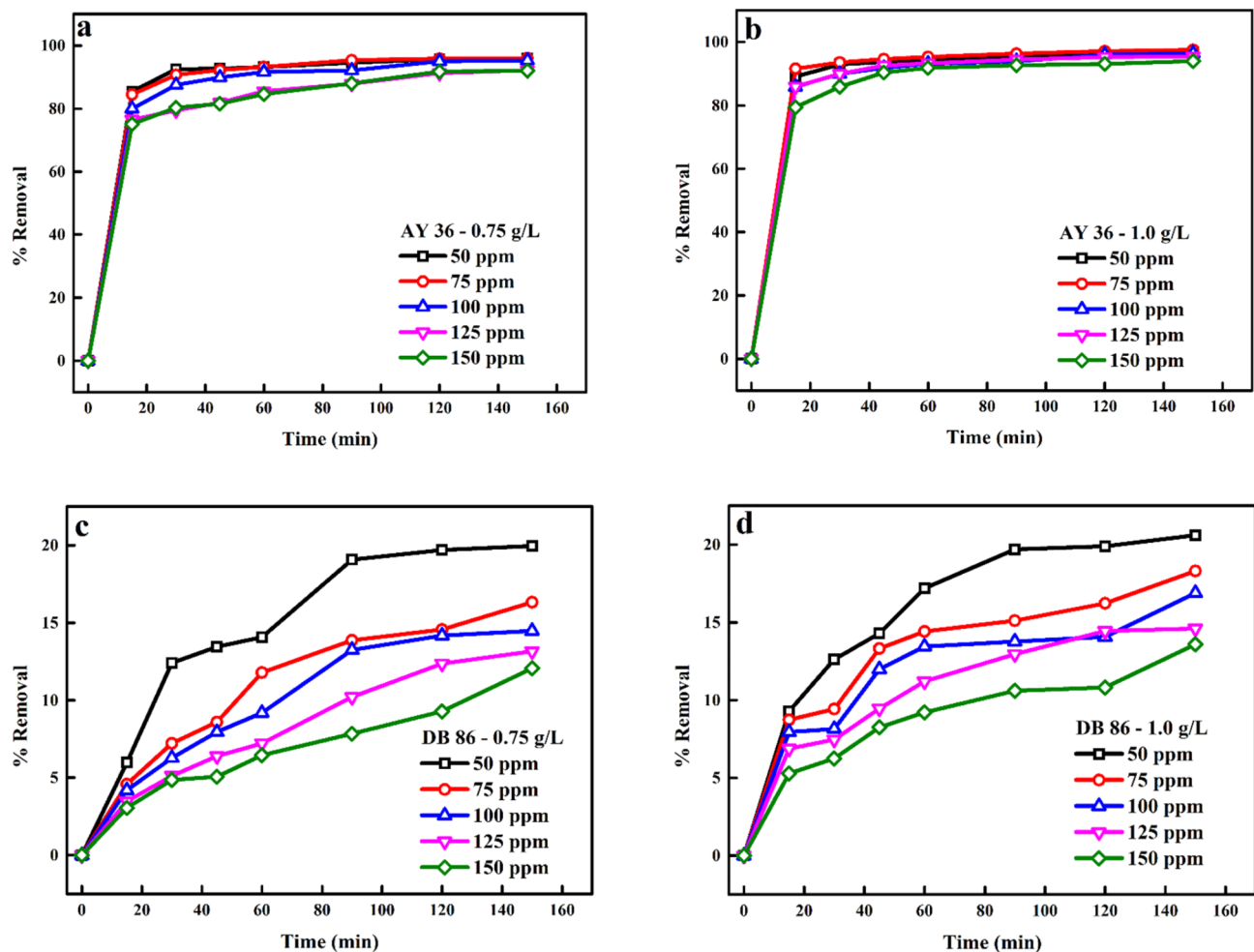
Fig. 10. Influence of initial concentrations on the removal of (a) AY36 dye using 0.75 g/L biochar dosage, (b) AY36 dye using 1.0 g/L biochar dosage, (c) DB86 dye using 0.75 g/L biochar dosage and (d) DB86 dye using 1.0 g/L biochar dosage.

isotherm model that incorporates three factors. It blends elements from the LGM and FDM equation, hence the mechanism of sorption is a blend and does not follow an ideal monolayer sorption. The linearized form of this model is given by Eq. (14)[103].

$$\ln \frac{C_e}{q_e} = \beta \ln C_e - \ln A \tag{14}$$

β, and A represents dimensionless RP exponent parameter that lies between 0 and 1 and RPM constant (L/mg)[104].

The linear plots of all models are given in Fig. 12. The parameters determined by all models in Tables 7 and 8 show that the LGM had higher R^2 values than the FDM and RPM R^2 values, except for RPM R^2 values for 1.75 g/L dosage for adsorption of DB86 dye. Because the dye molecules were evenly and uniformly distributed over the biosorbent's porous surface, the LGM provided the best description of the biosorption of both dye molecules to the biosorbent. The determined biosorption capacities for both dyes were 270.27 mg/g (AY36 dye) and 36.23 mg/g (DB86 dye). The biosorption process suggested that both dyes were biosorbed to the biosorbent in a monolayer. When compared to various biosorbents that have been utilized throughout the years for the confiscation of both dyes, it was found from the considered literature summarised in Table 9 that the biosorption of both dyes to the produced biosorbent was outstanding. The relatively lower adsorption capacity for DB86 dye compared to AY36 dye (q_m values of 36.23 for DB86 and 270.27 for AY36 dye) (Table 9) may be attributed to the molecular structure (reduced dye molecular structures are readily adsorbed into the pores of porous materials), size, and FGs (electron density of the anionic functional and the steric effect of the dye molecules performance a major role in the adsorption rate determination) of the dyes. Variations in these factors may impact how the dye molecules and the DRB-S biosorbent interact[105–107].
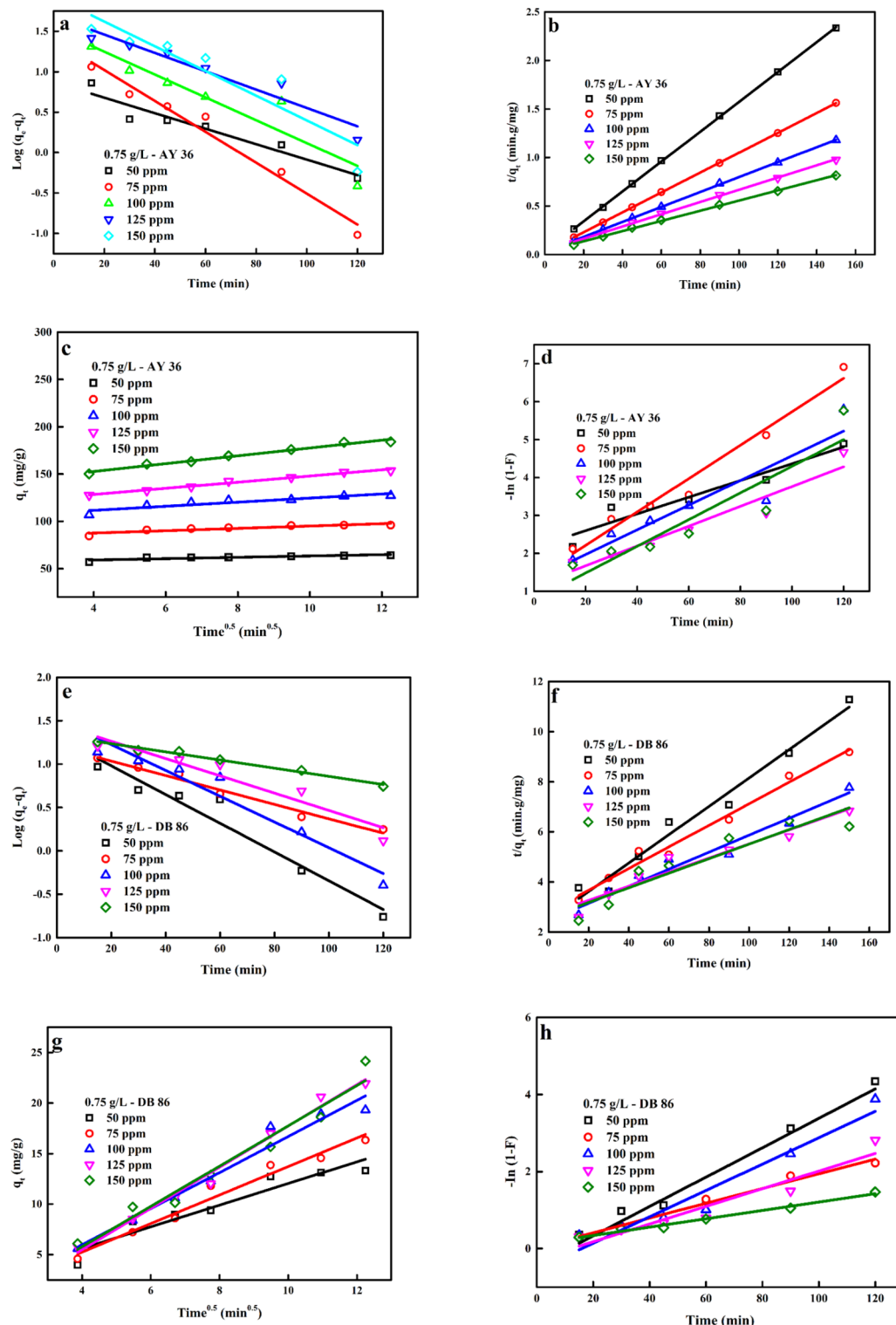
Fig. 11. Linear plots of (a–d) PFOM, PSOM, IDM and FIM for the biosorption of AB36 dye, (e–h) PFOM, PSOM, IDM and FIM for the biosorption of DB86 dye.

Adsorption mechanism of MB dye by DRB-S

Figure 13 explains the likely mechanism by which DRB-S absorbed the AY36 dye and DB86 dye ions. Following the 85% H_2SO_4 dehydration of the DPSPs (Delonix regia raw material). According to FTIR analysis, various FGs, including C=O, COOH, C–O–C, hydroxyl O–H, C–S, and SH groups, developed on the surface of the adsorbent (DRB-S). Because of the electrostatic interaction between the oxygen lone pair on the DRB-S surface and the positive charge on the sulphur atom of the AY36 dye and DB86 dye, the adsorption mechanism of the AY36 dye

Parameter			PFOM			PSOM			
DRB-S Dosage	AY36 (ppm)	q_e (exp.)	q_e (calc.)	$k_2 \times 10^3$	R^2	q_e (calc.)	$k_2 \times 10^3$	h	R^2
0.75 g L^{-1}	50	64.27	7.45	22.11	0.923	64.94	6.83	28818.44	1.000
	75	95.97	25.42	43.99	0.974	98.04	4.15	39840.64	1.000
	100	127.10	34.05	32.68	0.878	129.87	2.09	35211.27	1.000
	125	153.62	48.67	26.25	0.925	158.73	1.06	26737.97	0.999
	150	184.07	84.55	35.24	0.854	192.31	0.84	30959.75	0.999
1.0 g L^{-1}	50	48.78	4.56	16.81	0.958	49.26	9.56	23201.86	1.000
	75	73.13	6.71	24.87	0.984	73.53	8.64	46728.97	1.000
	100	96.40	16.37	2.72	0.921	98.04	3.69	35460.99	1.000
	125	119.31	19.28	33.62	0.985	120.48	3.94	57142.86	1.000
	150	141.00	23.10	26.02	0.917	142.86	2.33	47619.05	1.000
1.25 g L^{-1}	50	39.25	3.27	15.66	0.936	39.53	12.93	20202.02	1.000
	75	58.73	4.96	28.56	0.949	59.17	13.41	46948.36	1.000
	100	77.93	8.93	25.79	0.962	78.74	6.58	40816.33	1.000
	125	97.06	10.62	23.26	0.940	98.04	4.95	47619.05	1.000
	150	114.13	26.43	42.84	0.988	116.28	3.54	47846.89	1.000
1.5 g L^{-1}	50	32.76	2.32	15.43	0.933	32.89	18.41	19920.32	1.000
	75	49.09	2.49	20.27	0.987	49.26	20.40	49504.95	1.000
	100	65.47	2.67	19.11	0.965	65.79	8.99	38910.51	1.000
	125	81.56	5.55	21.65	0.940	81.97	9.42	63291.14	1.000
	150	97.07	8.89	20.50	0.889	98.04	5.45	52356.02	1.000
1.75 g L^{-1}	50	28.20	1.51	13.36	0.819	28.33	27.33	21929.82	1.000
	75	42.16	1.43	7.60	0.580	42.19	23.02	40983.61	1.000
	100	56.11	2.96	18.88	0.942	56.50	16.32	52083.33	1.000
	125	70.11	4.61	23.03	0.949	70.42	11.93	59171.60	1.000
	150	83.95	6.80	20.73	0.845	84.75	7.25	52083.33	1.000

Table 3. Comparison of the PFO and PSO rate constants and calculated parameters for different initial AY36 dye concentrations.

and DB86 dye ions in an acidic medium (pH 1.5) can be accomplished through physical interaction. Once the surface charge became positive, the acidic pH of the acidic medium attracted ions.

In an acidic environment, the surface of biochar picks up a positive charge, which attracts negatively charged dye molecules[111–113]. Additionally, the negative ions in the solution interact with the FGs of positive ions on the surface of the DRB-S. Additionally, dye molecules are more soluble at an acidic pH, facilitating their diffusion through the pores in the DRB-S and their attachment to the adsorption sites. Biochar-S is an excellent method for removing color from industrial effluent because the acidic pH is essential for encouraging the adsorption of AY36 dye and DB86 dye molecules onto the material. The most significant process is the adsorption of ionizable organic molecules to the positively charged surface of the biochar via electrostatic interaction[113]. How successfully an aqueous solution attracts or repels impurities depends on its pH and ionic strength[113,114].

Furthermore, the pH of the solution influences the capacity of organic contaminants in industrial effluent to adsorb[115]. Parshetti et al.'s study[116] examined the use of food waste-derived biochar in the adsorption of textile colours in wastewater. They found that an alkaline pH enhanced the adsorption of dyes. The significant interaction between the negatively charged sites on the biochar surface and the positively charged dyes explained it[117]. However, since there was an excess of H⁺ at pH 1.5, which competed with the positive charges of the dye, it was less successful at adsorbing organic dye[116]. Tsai and Chen[117] and Xu et al.[118] have noted that pH impacts biochar's capacity to absorb materials. As a result, the charged sites are altered by the pH of the solution, which alters the ability of organic and inorganic contaminants from industrial effluent to adsorb on biochar[119–122]. The hydrogen bonding among hydrogen donating OH groups on the DRB-S surface and nitrogen or oxygen atoms in the dyes (hdrogen acceptors) are termed dipole-dipole hydrogen bonding. Another probalbe hydrogen bonding interaction is the Yoshide bonding which exists between the aromatic rings present in the dyes and the OH groups that exist on the surface of the DRB-S adsorbent. Also, the existence of electron accepting aromatic rings on the dyes and electron donating oxygen groups on the biosorbent surface may give rise to the n-π interaction. The adsorption mechanism can also explained by π -π interaction which involved the intermolecular force of attraction between the organic molecules containing benzene rings or thr C=C bonds[123,124].

Regeneration study

Much research has demonstrated that regeneration processes, including thermal, microwave irradiation, moist air oxidation, microbial/biological, chemical/solvent, and others, are energy-efficient and can use little money, according to a recent study by Aragaw and Bogale[125]. NaOH and HCl were found to be among the best activating

Parameter		PFOM				PSOM			
DRB-S Dosage	DB86 (ppm)	q_e (exp.)	q_e (calc.)	k_1	R^2	q_e (calc.)	$k_2 \times 10^3$	h	R^2
0.75 g L^{-1}	50	12.99	11.70	18.19	0.994	17.06	1.14	330.71	0.996
	75	16.65	18.43	22.57	0.990	24.04	0.63	363.54	0.997
	100	20.71	22.43	20.04	0.943	30.77	0.43	406.92	0.992
	125	22.56	26.22	19.81	0.955	35.84	0.30	386.92	0.973
	150	23.07	21.19	12.44	0.992	33.44	0.34	382.66	0.927
1.0 g L^{-1}	50	10.26	7.60	24.64	0.998	11.81	3.69	514.32	1.000
	75	13.52	10.30	23.95	0.990	15.48	2.78	666.93	0.999
	100	15.85	9.67	18.19	0.989	17.67	2.64	823.93	0.996
	125	17.24	14.64	27.87	0.979	19.76	2.28	890.08	0.999
	150	18.52	17.68	24.41	0.960	22.47	1.31	663.44	0.995
1.25 g L^{-1}	50	8.46	3.72	26.02	0.973	8.98	11.68	940.82	1.000
	75	10.99	5.50	29.48	0.984	11.76	7.48	1034.98	1.000
	100	12.85	4.25	13.82	0.868	13.33	11.18	1986.89	0.999
	125	14.70	3.32	20.27	0.790	15.17	7.55	1738.53	0.997
	150	15.15	4.64	23.26	0.952	15.75	9.39	2329.37	1.000
1.5 g L^{-1}	50	7.19	1.64	11.28	0.927	7.30	19.74	1053.52	0.997
	75	9.36	2.46	24.64	0.989	9.65	19.97	1860.81	1.000
	100	10.84	2.65	20.73	0.894	11.17	15.72	1963.09	1.000
	125	12.46	3.59	15.66	0.919	12.87	9.63	1595.91	0.999
	150	13.11	4.34	16.58	0.964	13.64	7.90	1470.37	0.998
1.75 g L^{-1}	50	7.11	2.38	13.36	0.964	7.38	12.58	684.98	0.994
	75	9.16	2.15	15.20	0.964	9.38	16.57	1457.94	0.998
	100	10.60	2.67	19.11	0.982	10.91	15.23	1810.94	0.999
	125	11.69	2.26	20.04	0.975	11.93	19.52	2779.32	1.000
	150	13.02	2.90	25.79	0.984	13.33	18.32	3256.27	1.000

Table 4. Comparison of the PFO and PSO rate constants and calculated parameters for different initial DB86 dye concentrations.

agents, exhibiting superior performance throughout the desorption process. It has been observed that chemical/solvent regeneration is employed more frequently when the adsorbents have many efficient adsorption-desorption cycles[125]. Desorption tests were conducted on the AY36 and DB86 dyes from the DRB-S adsorbent using 0.1 M NaOH as an elution desorption media. The concentrations of the dyes were measured, and the DRB-S was then reactivated using 0.1 M HCl. This was done to examine the viability and adsorbent reusability of the adsorption of AY36 and DB86 dyes. The percentage of dye desorption in this work reduced as the regeneration cycles increased (Fig. 14a). Six adsorption/desorption cycles have been examined using the regenerated DRB-S. The variations in adsorption and desorption were consistent across the cycles[40,41,43]. Nevertheless, after six cycles, it dropped by around 3.3% for DB86 dye and 8.59% for AY36 dye. DRB-S might be applied as a long-lasting water dye removal method for AY36 and DB86 dyes (Fig. 14b).

Conclusion

The present study aims to eliminate two hazardous dyes (AY36 and DB86 dyes) from the water cycle using DRB-S. The optimal pH for AY36 dye and DB86 dye adsorption to the DRB-S adsorbent was at pH 1.5. For the adsorption of AY36 and DB86 to DRB-S, equilibrium was attained at 30 and 90 min of reaction time interaction. The LGM and PSOM were found to excellently define the biosorption of both dye molecules to the biosorbent. The determined biosorption capacities for both dyes (AY36 and DB86) were 270.27 mg/g and 36.23 mg/g, respectively. Accordingly, this novel synthesized DRB-S adsorbent had an outstanding sorption capacity. It effectively removed AY36 and DB86 dyes, signifying their potential utilization for wastewater treatment and that they can be reused without any loss to their adsorption efficiency. To enhance the study's findings, it is recommended to further optimize adsorption conditions, especially for DB86 dye. Additionally, testing the adsorbent in real wastewater conditions and conducting pilot-scale studies would help evaluate its practical application. Lastly, examining the environmental impact and potential toxicity of the dye-laden adsorbent is crucial to ensure the safety and sustainability of the biosorption process for wastewater treatment.

DRB-S dosage	AY36 (ppm)	IDM			FIM	
		K_{dif}	C	R^2	K_{FD}	R^2
0.75 g L^{-1}	50	0.708	56.240	0.778	0.022	0.923
	75	1.238	82.553	0.826	0.044	0.974
	100	2.163	102.820	0.854	0.033	0.878
	125	3.275	115.160	0.985	0.026	0.925
	150	4.131	136.200	0.978	0.035	0.854
1.0 g L^{-1}	50	0.438	43.544	0.913	0.017	0.958
	75	0.514	67.210	0.956	0.025	0.984
	100	1.173	82.968	0.926	0.027	0.925
	125	1.313	104.910	0.851	0.034	0.985
	150	2.311	115.770	0.783	0.026	0.917
1.25 g L^{-1}	50	0.333	35.265	0.880	0.016	0.936
	75	0.334	54.908	0.954	0.029	0.949
	100	0.722	69.768	0.896	0.026	0.962
	125	1.015	85.682	0.824	0.023	0.940
	150	1.552	97.532	0.807	0.043	0.988
1.5 g L^{-1}	50	0.239	29.899	0.878	0.015	0.933
	75	0.230	46.420	0.923	0.020	0.987
	100	0.503	59.592	0.917	0.019	0.965
	125	0.557	75.290	0.826	0.022	0.640
	150	0.990	86.000	0.748	0.020	0.889
1.75 g L^{-1}	50	0.172	26.141	0.838	0.013	0.819
	75	0.150	40.123	0.736	0.008	0.580
	100	0.283	52.808	0.890	0.019	0.942
	125	0.460	64.998	0.784	0.023	0.949
	150	0.696	76.047	0.824	0.021	0.845

Table 5. Comparison of the IDM and FIM rate constants and calculated parameters for different initial AY36 dye concentrations.

Sorbent dose	DB86 (ppm)	IDM			FIM	
		K_{dif}	C	R^2	K_{FD}	R^2
0.75 g L⁻¹	50	1.039	0.567	0.983	0.018	0.994
	75	1.464	− 0.503	0.981	0.023	0.990
	100	1.840	− 1.309	0.994	0.020	0.984
	125	2.070	− 2.528	0.997	0.020	0.955
	150	1.952	− 2.096	0.986	0.013	0.992
1.0 g L⁻¹	50	0.637	3.044	0.919	0.029	0.998
	75	0.808	4.183	0.964	0.024	0.990
	100	0.879	5.393	0.963	0.018	0.989
	125	1.023	5.559	0.957	0.028	0.979
	150	1.288	3.425	0.987	0.024	0.960
1.25 g L⁻¹	50	0.323	4.865	0.851	0.026	0.973
	75	0.458	5.980	0.808	0.030	0.984
	100	0.413	8.284	0.703	0.020	0.790
	125	0.468	9.082	0.829	0.014	0.868
	150	0.456	10.064	0.816	0.023	0.952
1.5 g L⁻¹	50	0.169	5.041	0.938	0.011	0.927
	75	0.215	6.946	0.890	0.025	0.989
	100	0.285	7.638	0.805	0.021	0.894
	125	0.381	7.953	0.879	0.016	0.919
	150	0.430	7.997	0.920	0.017	0.964
1.75 g L⁻¹	50	0.215	4.371	0.985	0.014	0.964
	75	0.190	6.782	0.991	0.015	0.964
	100	0.223	7.916	0.990	0.019	0.982
	125	0.186	9.472	0.982	0.020	0.975
	150	0.211	10.279	0.975	0.026	0.984

Table 6. Comparison of the IDM and FIM rate constants and calculated parameters for different initial DB86 dye concentrations.
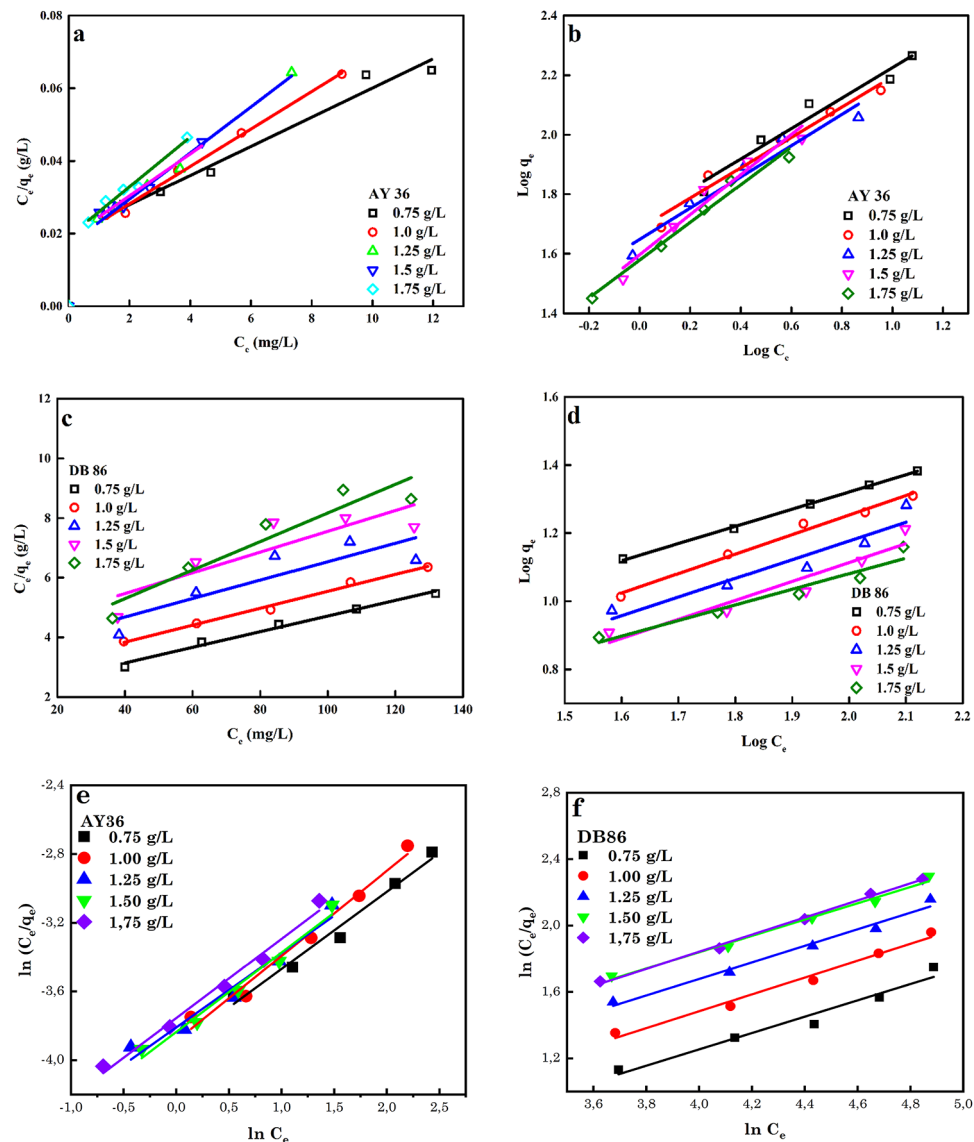
Fig. 12. Linear plots of (a and b) LGM and FDM for the biosorption of AB36 dye, (c and d) LGM and FDM for the biosorption of DB86 dye and (e and f) Redlich model for the biosorption of AB36 and DB86 dyes.

Isotherm	Isotherm	DRB-S concentrations				
Model	Parameters	0.75 g/L	1 g/L	1.25 g/L	1.5 g/L	1.75 g/L
LGM	q_m (mg/g)	270.27	192.31	144.93	142.86	120.48
	K_L x 10^3	0.2	0.3	0.5	0.5	0.6
	R^2	0.9967	0.9973	0.9984	0.9989	0.9973
FDM	K_F	0.53	0.52	0.50	0.47	0.46
	n	1.96	1.96	1.90	1.48	1.58
	R^2	0.9850	0.9810	0.9680	0.9760	0.9990
RPM	β	0.45	0.50	0.43	0.46	0.46
	A	1.37	1.36	1.34	1.35	1.32
	R^2	0.9775	0.9803	0.9598	0.9776	0.9848

Table 7. Deteremined LGM, FDM, and RPM constants and calculated parameters for AY36 dye utilizing different DRB-S dosage.

Isotherm	Isotherm	DRB-S concentrations				
Model	Parameters	0.75 g/L	1 g/L	1.25 g/L	1.5 g/L	1.75 g/L
LGM	q_m (mg/g)	36.2300	28.0900	23.6400	20.7000	19.5700
	K_L x 10^3	0.01430	0.0149	0.0143	0.0135	0.0149
	R^2	0.97880	0.9981	0.9924	0.9961	0.9949
FDM	K_F	18.300	16.700	15.400	14.500	15.300
	n	2.0430	1.7310	1.3710	1.1300	1.232
	R^2	0.9630	0.982	0.9830	0.9910	0.994
RPM	β	0.4900	0.5100	0.5000	0.4900	0.5200
	A	0.7200	0.5500	0.3200	0.1200	0.2200
	R^2	0.9608	0.9833	0.9830	0.9897	0.9966

Table 8. Determined LGM, FDM, and RPM constants and calculated parameters for DB86 dye using different DRB-S dosage.

Biosorbents	q_m (mg/g)	References
DRB-S	270.27 (AY36)	This study
DRB-S	36.23 (DB86)	This study
Cellulose hydrogel	53.76 (DB86)	[108]
Manioc husk	6.1 (DB86)	[109]
Alginate-encapsulated activated carbon	21.6 (DB86)	[110]
N-doping activated carbons from fish waste and sawdust	232.56 (AY36)	[80]

Table 9. Comparison of the maximum biosorption capacities of DRB-S employed for removing AY36 and DB86 dyes.
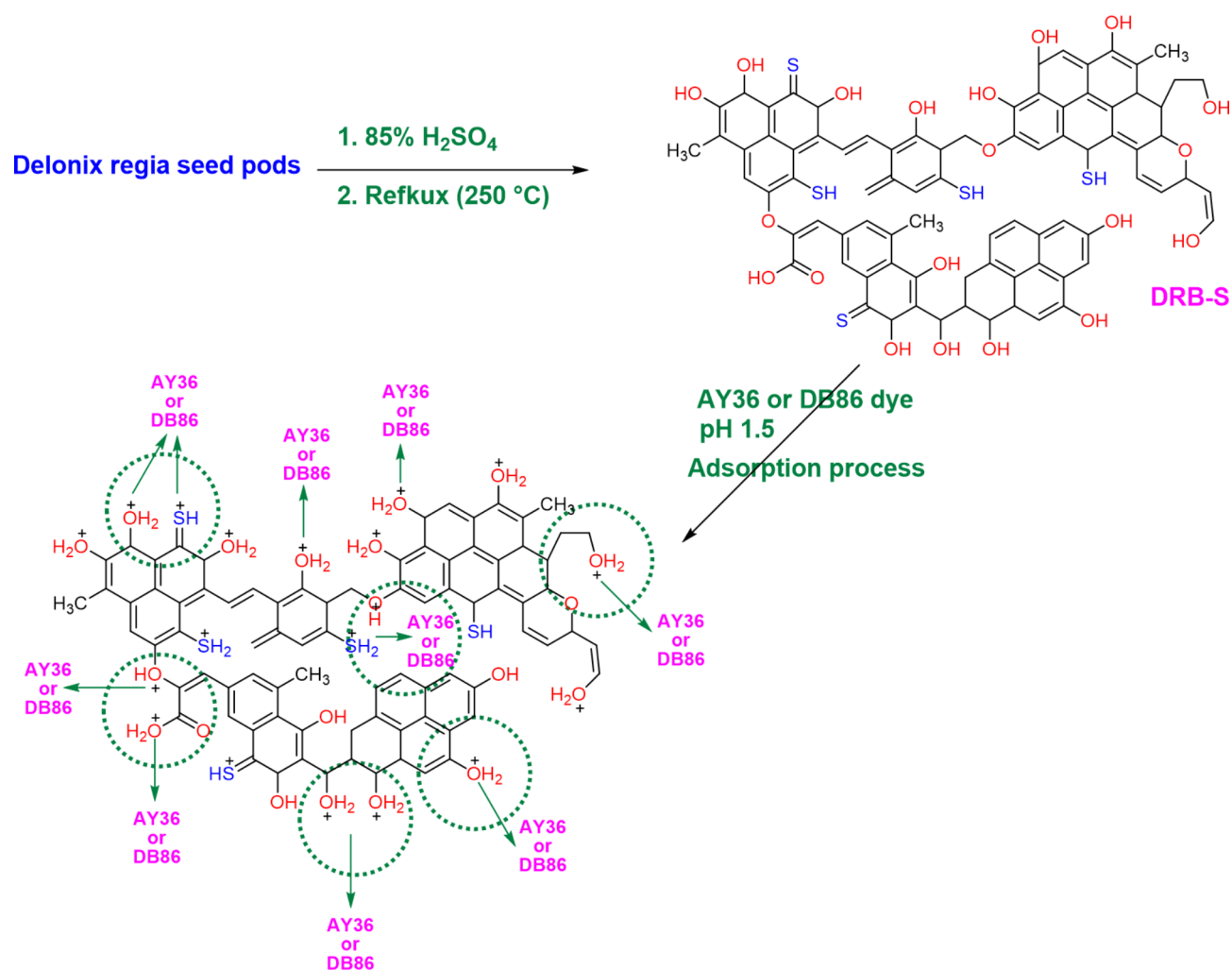
Fig. 13. The likely mechanism by which the AY36 and DB86 dyes are adsorbed onto the DRB-S.
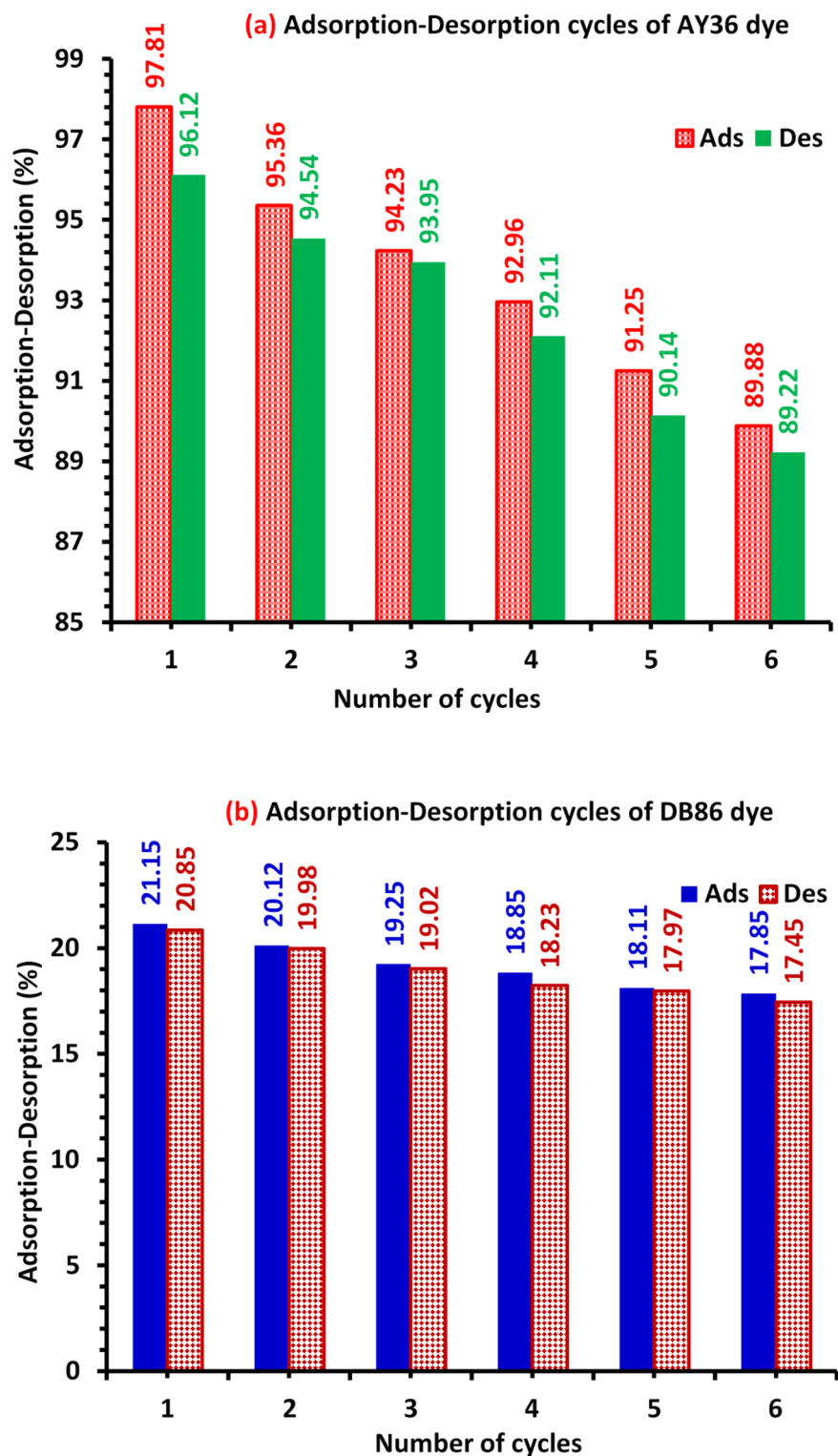
Fig. 14. Renewal study of (a) AY36 dye and (b) DB86 dye adsorption-desorption by DRB-S adsorbent using dye C_0 (100 ppm) and 1.0 g/L DRB-S dose at room temperature.

Data availability

Data will be available upon request from the corresponding author.

References

1. Eldeeb, T. M. et al. Biosorption of acid brown 14 dye to mandarin-CO-TETA derived from mandarin peels. *Biomass Convers. Biorefinery* **2022**, 1–21 (2022).
2. Srivatsav, P. et al. Biochar as an eco-friendly and economical adsorbent for the removal of colorants (dyes) from aqueous environment: a review. *Water* **12**, 3561 (2020).
3. Aigbe, U. O. et al. A facile review on the sorption of heavy metals and dyes using bionanocomposites. *Adsorpt. Sci. Technol.* **8030175**, 1–36 (2022).
4. Aigbe, U. O. et al. Fly Ash-based adsorbent for adsorption of heavy metals and dyes from aqueous solution: a review. *J. Mater. Res. Technol.* **14**, 2751–2774 (2021).
5. Nithyalakshmi, B., Saraswathi, R. & Praveen, S. Removal of basic fuchsin red dye by turmeric leaf waste biochar: batch adsorption studies, isotherm kinetics and RSM studies. *Global NEST J.* **25**(1), 17–27 (2022).
6. Eleryan, A. et al. Adsorption of Direct Blue 106 dye using zinc oxide nanoparticles prepared via green synthesis technique. *Environ. Sci. Pollut. Res.* **30**(26), 69666–69682 (2023).
7. Neolaka, Y. A. B. et al. Potential of activated Carbon from various sources as a low-cost adsorbent to remove Heavy metals and Synthetic dyes. *Results Chem.* **5**, 100711 (2023).
8. Saigl, Z. M. Various adsorbents for removal of rhodamine b dye: a review. *Indones J. Chem.* **21**, 1039–1056 (2021).
9. El Messaoudi, N. et al. Advancements in adsorption and photocatalytic degradation technologies of brilliant green from water: current status, challenges, and future prospects. *Mater. Today Chem.* **42**, 102399 (2024).
10. El Messaoudi, N. et al. A critical review of Allura red removal from water: advancements in adsorption and photocatalytic degradation technologies, and future perspectives. *J. Environ. Chem. Eng.* **2024**, 114843 (2024).
11. Kurtulbaş, E., Ciğeroğlu, Z., Şahin, S., El Messaoudi, N. & Mehmeti, V. Monte Carlo, molecular dynamic, and experimental studies of the removal of malachite green using g-C3N4/ZnO/Chitosan nanocomposite in the presence of a deep eutectic solvent. *Int. J. Biol. Macromol.* **274**, 133378 (2024).
12. Yao, W., Luo, C., Wu, J. & Hou, G. Degradation of acid yellow 36 azo dye from textile wastewater using vanadium-doped TiO2 photonanocatalyst. *Int. J. Electrochem. Sci.* **17**(9), 220916 (2022).
13. Kumar, D. & Gupta, S. K. Electrochemical oxidation of direct blue 86 dye using MMO coated Ti anode: modelling, kinetics and degradation pathway. *Chem. Eng. Process.-Process Intensif.* **181**, 109127 (2022).
14. Shoaib, A. G., El Nemr, A., Ramadan, M. S., Masoud, M. S. & Sikaily, E. A Composite fabrication and characterization of crosslinked polyaniline/Pterocladia capillacea-activated carbon for adsorption of direct blue-86 dye from water. *Polym. Bull.* **80**(9), 10393–10428 (2023).
15. Sharma, U. K. et al. Ameliorating efficacy of eugenol against metanil yellow induced toxicity in albino Wistar rats. *Food Chem. Toxicol.* **126**, 34–40 (2019).
16. Naseri, S. et al. Optimisation and modelling of direct blue 86 removal from aqueous solutions by cationic surfactant enhanced ultrafiltration. https://doi.org/10.1080/03067319.2021.1982923 (2021).
17. El Messaoudi, N. et al. Future trends and innovations in the treatment of industrial effluent. In *Advances in Chemical Pollution, Environmental Management and Protection* (Elsevier, 2024).
18. Ihaddaden, S., Aberkane, D., Boukerroui, A. & Robert, D. Removal of methylene blue (basic dye) by coagulation-flocculation with biomaterials (bentonite and Opuntia ficus indica). *J. Water Process. Eng.* **49**, 102952 (2022).
19. Anil, G., Scaria, J. & Nidheesh, P. V. Removal of synthetic dye from aqueous solution using $MnFe_2O_4$-GO catalyzed heterogeneous electro-fenton process. *Water* **14**, 3350 (2022).
20. Dung, N. T. N. N. et al. A comprehensive study on the heterogeneous electro-Fenton degradation of tartrazine in water using $CoFe_2O_4$/carbon felt cathode. *Chemosphere* **287**, 132141 (2022).
21. Liu, W. et al. Effective extraction of Cr(VI) from hazardous gypsum sludge via controlling the phase transformation and chromium species. *Environ. Sci. Technol.* **52**(22), 13336–13342. https://doi.org/10.1021/acs.est.8b02213 (2018).
22. Liu, W. et al. Different pathways for Cr(III) oxidation: implications for Cr(VI) reoccurrence in reduced chromite ore processing residue. *Environ. Sci. Technol.* **54**(19), 11971–11979. https://doi.org/10.1021/acs.est.0c01855 (2020).
23. Sun, L. et al. Ultralight and superhydrophobic perfluorooctyltrimethoxysilane modified biomass carbonaceous aerogel for oil-spill remediation. *Chem. Eng. Res. Des.* **174**, 71–78. https://doi.org/10.1016/j.cherd.2021.08.002 (2021).
24. Helmy, Q., Suryawan, I. W. K. & Notodarmojo, S. Ozone-based processes in dye removal. In *Advanced Oxidation Processes in Dye-Containing Wastewater. Sustainable Textiles: Production, Processing, Manufacturing & Chemistry* (eds Muthu, S. S. & Khadir, A.) (Springer, 2022). https://doi.org/10.1007/978-981-19-0882-8_6.
25. Hassaan, M. A., El Nemr, A. & Madkour, F. F. Testing the advanced oxidation processes on the degradation of Direct Blue 86 dye in wastewater. *Egypt. J. Aquat. Res.* **43**, 11–19. https://doi.org/10.1016/j.ejar.2016.09.006 (2017).
26. Hassaan, M. A., El Nemr, A. & Madkour, F. F. Advanced oxidation processes of mordant violet 40 dye in freshwater and seawater. *Egypt. J. Aquat. Res.* **43**, 1–9 https://doi.org/10.1016/j.ejar.2016.09.004 (2017).
27. El Nemr, A., Hassaan, M. A. & Madkour, F. F. Advanced oxidation process (AOP) for detoxification of acid red 17 dye solution and degradation mechanism. *Environ. Process.* **5**, 95–113. https://doi.org/10.1007/s40710-018-0284-9 (2018).
28. Hashem, A. H., Saied, E. & Hasanin, M. S. Green and ecofriendly bio-removal of methylene blue dye from aqueous solution using biologically activated banana peel waste. *Sustain. Chem. Pharm.* **18**, 100333 (2020).
29. Cheng, J., Cheng, X., Wang, Z. & Jen, T. Enhanced hydrogen storage and CO2 capture capacities on carbon aerogels from Ni-N co-doping. *Fuel* **372**, 132271. https://doi.org/10.1016/j.fuel.2024.132271 (2024).
30. El Nemr, A., El Sikaily, A., Khaled, A. & Abdelwahab, O. Removal of toxic chromium (VI) from aqueous solution by activated carbon using *Casuarina Equisetifolia*. *Chem. Ecol.* **23**(2), 119–129 (2007).
31. El Sikaily, A., El Nemr, A. & Khaled, A. Copper sorption onto dried red alga *Pterocladia capillacea* and its activated carbon. *Chem. Eng. J.* **168**, 707–714. https://doi.org/10.1016/j.cej.2011.01.064 (2011).
32. El-Nemr, M. A., Ismail, I. M. A., Abdelmonem, N. M., El Nemr, A. & Ragab, S. Amination of biochar derived from Watermelon peel by Triethylenetetramine and ammonium hydroxide for toxic chromium removal enhancement. *Chin. J. Chem. Eng.* **36**, 199–222 (2021).
33. El Nemr, A., Shoaib, A. G. M., El Sikaily, A., Mohamed, A. E. D. A. & Hassan, A. F. Evaluation of cationic Methylene blue dye removal by high surface area mesoporous nano activated carbon derived from *Ulva lactuca*. *Environ. Process.* **8**(1), 311–332. https://doi.org/10.1007/s40710-020-00487-8 (2021).
34. Sahlabji, T. et al. High surface area microporous activated carbon from *Pisum sativum* peels for hexavalent chromium removal from aquatic environment. *Toxin Rev.* **41**(2), 639–649. https://doi.org/10.1080/15569543.2021.1908361 (2022).
35. Yılmaz, M. et al. The Use of Mandarin-Biochar-O3-TETA (MBT) produced from Mandarin peels as a natural adsorbent for the removal of Acid Red 35 (AR35) dye from Water. *Environ. Process.* **9**, 44. https://doi.org/10.1007/s40710-022-00592-w (2022).
36. El Nemr, A. et al. Utilization of green alga *Ulva lactuca* for sustainable production of meso-micro porous nano activated carbon for adsorption of Direct Red 23 dye from aquatic environment. *Carbon Lett.* **32**, 153–168. https://doi.org/10.1007/s42823-021-00262-1 (2022).
37. El Nemr, A. et al. Microporous activated carbons with a high surface area of type I adsorption isotherm derived from sugarcane bagasse impregnated with zinc chloride. *Carbon Lett.* **32**, 229–249. https://doi.org/10.1007/s42823-021-00270-1 (2022).
38. El Nemr, A. et al. Microporous nano activated carbon type I derived from orange peel and its application for cr(VI) removal from aquatic environment. *Biomass Convers. Biorefinery* **12**, 5125–5143. https://doi.org/10.1007/s13399-020-00995-5 (2022).

23

39. Shoaib, A. G. M., El-Sikaily, A., El Nemr, A., Mohamed, A. E. D. A. & Hassan, A. F. Testing the carbonization condition for high surface area preparation of activated carbon followed type IV from green alga Ulva lactuca. *Biomass Convers. Biorefinery.* **12**, 3303–3318. https://doi.org/10.1007/s13399-020-00823-w (2022).

40. El Nemr, A. et al. Utilization of sugarcane bagasse/ZnCl₂ for sustainable production of microporous nano activated carbons of type I for toxic Cr(VI) removal from aqueous environment. *Biomass Convers. Biorefinery* 13, 1581–1600. https://doi.org/10.1007/s13399-021-01445-6 (2023).

41. El Nemr, A. et al. Utilization of Citrus aurantium peels for sustainable production of high surface area type I microporous nano activated carbons. *Biomass Convers. Biorefinery.* **13**, 1613–1631. https://doi.org/10.1007/s13399-021-01457-2 (2023).

42. El Nemr, A. *Textiles: Types, Uses and Production Methods* (Nova Science Publishers, Inc., 2012).

43. El Nemr, A. Non-conventional textile waste water treatment. In *Pollution Science, Technology and Abatement Series* (Nova Science Publishers, Inc., 2012). https://www.amazon.com/Non-Conventional-Treatment-Pollution-Technology-Abatement/dp/1621000796.

44. El Nemr, A. Impact, monitoring and management of environmental pollution. In *Pollution Science, Technology and Abatement Series* (Nova Science Publishers, Inc., 2010).

45. El Nemr, A. Environmental pollution and its relation to climate change. In *Pollution Science, Technology and Abatement Series* (Nova Science Publishers, Inc., 2011).

46. Lin, Y. T., Kao, F. Y., Chen, S. H., Wey, M. Y. & Tseng, H. H. A facile approach from waste to resource: reclaimed rubber-derived membrane for dye removal. *J. Taiwan. Inst. Chem. Eng.* **112**, 286–329 (2020).

47. Eleryan, A. et al. Biochar-C-TETA as a superior adsorbent to Acid Yellow 17 dye from water: isothermal and kinetic studies. *J. Chem. Technol. Biotechnol.* **98**(10), 2415–2428. https://doi.org/10.1002/jctb.7466 (2023).

48. Mohamed, S. M. I., Güner, E. K., Yılmaz, M., Nemr, E. & A Removal of Cr6 + ions and mordant Violet 40 dye from Liquid Media using Pterocladia capillacea red algae derived activated carbon-iron oxides. *Sci. Rep.* **13**, 18306. https://doi.org/10.1038/s41598-023-45464-x (2023).

49. Hassaan, M. A. et al. Isotherm and kinetic investigations of sawdust based biochar modified by ammonia to remove methylene blue from water. *Sci. Rep.* **13**(2023), 12724 (2023).

50. Hassaan, M. A. et al. Improved Methylene Blue adsorption from an aqueous medium by ozone-triethylenetetramine modification of Sawdust-Based Biochar. *Sci. Rep.* **13**(2023), 12431. https://doi.org/10.1038/s41598-023-39495-7 (2023).

51. Eleryan, A. et al. Kinetic and isotherm studies of acid orange 7 dye absorption using sulphonated mandarin biochar treated with TETA. *Biomass Convers. Biorefinery* **2023**, 1–12. https://doi.org/10.1007/s13399-023-04089-w (2023).

52. Eldeeb, T. M. et al. Adsorption of methylene blue dye on sawdust ozone, purified sawdust, and sonicated sawdust biochars. *Biomass Convers. Biorefin.* **12**(7), 2022. https://doi.org/10.1007/s13399-022-03015-w (2022).

53. Meky, A. I. et al. Cube-shaped Cobalt-doped zinc oxide nanoparticles with increased visible-light-driven photocatalytic activity achieved by green co-precipitation synthesis. *Sci. Rep. 13*(1), 19329 (2023).

54. Hassaan, M. A. et al. Application of multi-heteroatom doping biochar in a newly proposed mechanism of electron transfer in biogas production. *Chem. Eng. J.* **470**, 144229 (2023).

55. Eldeeb, T. M., El Nemr, A., Khedr, M. H. & El-Dek, S. I. Novel bio-nanocomposite for efficient copper removal. *Egypt. J. Aquat. Res.* **47**(3), 261–267. https://doi.org/10.1016/j.ejar.2021.07.002 (2021).

56. Eleryan, A. et al. Mandarin Biochar-TETA (MBT) prepared from *Citrus reticulata* peels for adsorption of Acid Yellow 11 dye from water. *Sci. Rep.* **12**, 17797 (2022).

57. Eldeeb, T. M. et al. Adsorption of Methylene Blue (MB) dye on ozone, purified and sonicated Sawdust biochars. *Biomass Convers. Biorefinery* **2022**, 1–23 (2022).

58. Nwokocha, L. M. Galactomannans. In *Handbook of Hydrocolloids* 273–293 (Woodhead Publishing, 2021).

59. Gregg, S. J. & Sing, K. S. W. *Adsorption Surface Area and Porosity* 2nd edn (Academic Press INC., 1982).

60. Rouquerol, F., Rouquerol, J. & Sing, K. S. W. *Adsorption by Powders and Porous Solids* (Academic Press INC., 1999).

61. Barrett, E. P., Joyner, L. G. & Halenda, P. P. The determination of pore volume and area distributions in porous substances. I. computations from nitrogen isotherms. *J. Am. Chem. Soc.* **73**(1), 373–380 (1951).

62. El-Nemr, M. A., Yılmaz, M., Ragab, S., Nemr, E. & A Biochar-SO prepared from pea peels by dehydration with Sulfuric Acid improves the adsorption of Cr⁶⁺ from Water. *Biomass Convers. Biorefinery* **14**, 2601–2619. https://doi.org/10.1007/s13399-022-02378-4 (2024).

63. El-Nemr, M. A., Yılmaz, M., Ragab, S. & Nemr, E. Watermelon peels Biochar-S for Adsorption of Cu²⁺ from water. *Desalination Water Treat.* **261**, 195–213. https://doi.org/10.5004/dwt.2022.28506 (2022).

64. Hassaan, M. A. et al. Synthesis, characterization, optimization and application of Pisum sativum peels S and N-doping biochars in the production of biogas from Ulva lactuca. *Renew. Energy* **221**, 119747. https://doi.org/10.1016/j.renene.2023.119747 (2024).

65. Hassaan, M. A. & Nemr, E. A. Classification and identification of different minerals in the Mediterranean sediments using PSA, FTIR, and XRD techniques. *Mar. Pollut. Bull.* **173**, 113070 (2021).

66. Eleryan, A. et al. Copper (II) ion removal by chemically and physically modified sawdust biochar. *Biomass Convers. Bioref.* https://doi.org/10.1007/s13399-022-02918-y (2022).

67. El Sikaily, A., El Nemr, A. & Khaled, A. Copper sorption onto dried red alga Pterocladia capillacea and its activated carbon. *Chem. Eng. J.* **168**, 707–714. https://doi.org/10.1016/j.cej.2011.01.064 (2011).

68. Rodrigues, S. C., Silva, M. C., Torres, J. A. & Bianchi, M. L. Use of magnetic activated carbon in a solid phase extraction procedure for analysis of 2, 4-dichlorophenol in water samples. *Water Air Soil Pollut.* **231**, 1–13 (2020).

69. George, G. & Saravanakumar, M. P.Facile synthesis of carbon-coated layered double hydroxide and its comparative characterisation with Zn–Al LDH: application on crystal violet and malachite green dye adsorption—isotherm, kinetics and Box-Behnken design. *Sci. Pollut. Res.* **25**, 30236–30254 (2018).

70. Saenko, N. S. The X-ray diffraction study of three-dimensional disordered network of nanographites: experiment and theory. *Phys. Procedia* **23**, 102–105 (2012).

71. Abraham, R. et al. Facile synthesis, growth process, characterisation of a nanourchin-structured MnO2 and their application on ultrasonic-assisted adsorptive removal of cationic dyes: a half-life and half-capacity concentration approach. *Ultrasonics Sonochem.* **49**, 175–189 (2018).

72. Meng, J., Li, S. & Niu, J. Crystallite structure characteristics and its influence on methane adsorption for different rank coals. *ACS Omega* **4**(24), 20762–20772 (2019).

73. Lee, S. M., Lee, S. H. & Roh, J. S. Analysis of activation process of carbon black based on structural parameters obtained by XRD analysis. *Crystals* **11**(2), 153 (2021).

74. Keppetipola, N. M. et al. Graphite-type activated carbon from coconut shell: a natural source for eco-friendly non-volatile storage devices. *RSC Adv.* **11**(5), 2854–2865 (2021).

75. Farma, R., Fatjrin, D., Awitdrus, A. & Deraman, M. Physical properties of activated carbon from fibers of oil palm empty fruit bunches by microwave assisted potassium hydroxide activation. In *AIP Conference Proceedings (Vol. 1801, No. 1)* (AIP Publishing, 2017).

76. Meng, J., Li, S., Niu, J. & Saenko, N. S. Crystallite structure characteristics and its influence on methane adsorption for different rank coals. *ACS omega* **4**(24), 20762–20772 (2012).

77. Said, A. A. et al. An efficient biosorption of direct dyes from industrial wastewaters using pretreated sugarcane bagasse. *Energy Environ. Eng.* **1**(1), 10–16 (2013).

78. Aigbe, U. O., Maluleke, R., Lebepe, T. C., Oluwafemi, O. S. & Osibote, O. A. Rhodamine 6G dye adsorption using magnetic nanoparticles synthesized with the support of *Vernonia Amygdalina* leaf extract (bitter leaf). (*J. Inorg. Organometal. Polym. Mater.* **2023**, 1–20 (2023).

79. Aigbe, U. O. et al. *Utility of Bionanocomposites for Wastewater Treatment* 8–11 (Bionanomaterials for Environmental and Agricultural Applications, 2021).

80. El-Nemr, M. A., Hassaan, M. A. & Ashour, I. Fabrication of N-doping activated carbons from fish waste and sawdust for Acid Yellow 36 dye removal from an aquatic environment. *Sci. Rep.* **13**(1), 5892 (2023).

81. Garg, D., Kumar, S., Sharma, K. & Majumder, C. B. Application of waste peanut shells to form activated carbon and its utilization for the removal of Acid Yellow 36 from wastewater. *Groundw. Sustain. Dev.* **8**, 512–519 (2019).

82. Thirunavukkarasu, A., Muthukumaran, K. & Nithya, R. Adsorption of acid yellow 36 onto green nanoceria and amine functionalized green nanoceria: comparative studies on kinetics, isotherm, thermodynamics, and diffusion analysis. *J. Taiwan Inst. Chem. Eng.* **93**, 211–225 (2018).

83. Hassaan, M. A. et al. Synthesis, characterization and synergistic effects of modified biochar in combination with α-Fe$_2$O$_3$ NPs on biogas production from red algae *Pterocladia capillacea*. *Sustainability* **13**, 9275. https://doi.org/10.3390/su13169275 (2021).

84. El Nemr, A. et al. Enhancement of biogas production from individually or co-digested green algae Cheatomorpha linum using ultrasound and ozonation treated biochar. *Ultrason. Sonochem.* **90**, 106197. https://doi.org/10.1016/j.ultsonch.2022.106197 (2022).

85. El-Nemr, M. A. et al. The use of biochar-NH$_2$ produced from watermelon peels as a natural adsorbent for the removal of Cu(II) ions from water. *Biomass Convers. Biorefinery* **14**, 1975–1991. https://doi.org/10.1007/s13399-022-02327-1 (2024).

86. Eleryan, A. et al. *Adsorption of Direct Blue 106 Dye Using Zinc Oxide Nanoparticles Prepared via Green Synthesis Technique* 1–17 (Environmental Science and Pollution Research, 2023).

87. Li, S. et al. Novel hydrophilic straw biochar for the adsorption of neonicotinoids: kinetics, thermodynamics, influencing factors, and reuse performance. *Environ. Sci. Pollut. Res.* **30**, 29143–29153. https://doi.org/10.1007/s11356-022-24131-0 (2023).

88. Hassaan, M. A. et al. Application of multi-heteroatom doping biochar in a newly proposed mechanism of electron transfer in biogas production. *Chem. Eng. J.* **470**, 144229. https://doi.org/10.1016/j.cej.2023.144229 (2023).

89. Di, J. et al. Adsorption behaviors and mechanisms of Cu^{2+}, Zn^{2+} and Pb^{2+} by magnetically modified lignite. *Sci. Rep.* **12**(1), 1394 (2022).

90. Aichour, A., Zaghouane-Boudiaf, H. & Khodja, H. D. Highly removal of anionic dye from aqueous medium using a promising biochar derived from date palm petioles: Characterization, adsorption properties and reuse studies. *Arab. J. Chem.* **15**(1), 103542 (2022).

91. Elkatory, M. R., Yılmaz, M., Hassaan, M. A. & El Nemr, A. Fabrication of date palm kernel Biochar-Sulfur (DPKB-S) for super adsorption of methylene blue dye from water. *Sci. Rep.* **14**, 6830. https://doi.org/10.1038/s41598-024-56939-w (2024).

92. El-Nemr, M. A. et al. Fabrication of Pea pods biochar-NH$_2$ (PBN) for absorption of toxic Cr^{6+} ion from water. *Appl. Water Sci.* **13**(2023), 194. https://doi.org/10.1007/s13201-023-02007-z (2023).

93. El-Nemr, M. A., Abdelmonem, N. M., Ismail, I. M. A., Ragab, S. & Nemr, E. The efficient removal of the hazardous azo dye Acid Orange 7 from water using modified biochar from pea peels. *Desalination Water Treat.* **203**, 327–355 (2020).

94. El-Nemr, M. A., Abdelmonem, N. M., Ismail, I. M. A., Ragab, S. & Nemr, E. Removal of Acid Yellow 11 dye using novel modified biochar derived from watermelon peels. *Desalination Water Treat.* **203**, 403–431 (2020).

95. Esmail, L. S. Optimization of toluidine blue biosorption in aqueous solutions using polyporus squamosus fungi as absorbent by response surface methodology. *Acad. J. Chem.* **6**(3), 60–68 (2021).

96. Ouettar, L. et al. Biosorption of triphenyl methane dyes (malachite green and crystal violet) from aqueous media by alfa (*Stipa tenacissima* L.) leaf powder. *Molecules* **28**(8), 3313 (2023).

97. El Nemr, A., El-Sikaily, A. & Khaled, A. Modeling of adsorption isotherms of Methylene Blue onto rice husk activated carbon. *Egypt. J. Aquat. Res.* **36**(3), 403–425 (2010).

98. El Nemr, A., El Sikaily, A., Khaled, A. & Abdelwahab, O. Removal of toxic chromium from aqueous solution, wastewater and saline water by marine red alga Pterocladia capillacea and its activated carbon. *Arab. J. Chem.* **8**, 105–117. https://doi.org/10.1016/j.arabjc.2011.01.016 (2015).

99. Chen, F. et al. Organosilica nanoparticles with an intrinsic secondary amine: an efficient and reusable adsorbent for dyes. *ACS Appl. Mater. Interfaces* **9**(18), 15566–15576 (2017).

100. Güleç, F. et al. A comprehensive comparative study on methylene blue removal from aqueous solution using biochars produced from rapeseed, whitewood, and seaweed via different thermal conversion technologies. *Fuel* **330**, 125428 (2022).

101. Tataru-Farmus, R. E., Cimpoesu, R., Nica, I. & Suteu, D. Biosorbent based on poly (vinyl alcohol)–tricarboxi-cellulose designed to retain organic dyes from aqueous media. *Polymers,* **15**(3), 715 (2023).

102. El Nemr, A. Pomegranate husk as an adsorbent in the removal of toxic chromium from wastewater. *Chem. Ecol.* **23**(5), 409–425 (2007).

103. Ayawei, N., Ebelegi, A. N. & Wankasi, D. Modelling and interpretation of adsorption isotherms. *J. Chem.* **2017**(1), 3039817 (2017).

104. Tsamo, C., Paltahe, A., Fotio, D., Vincent, T. A. & Sales, W. F. One-, two, and three-parameter isotherms, kinetics, and thermodynamic evaluation of Co (II) removal from aqueous solution using dead neem leaves. *Int. J. Chem. Eng.* **2019**(1), 6452672 (2019).

105. Haleem, A., Shafiq, A., Chen, S. Q. & Nazar, M. A comprehensive review on adsorption, photocatalytic and chemical degradation of dyes and nitro-compounds over different kinds of porous and composite materials. *Molecules* **28**(3), 1081 (2023).

106. Osagie, C. et al. Dyes adsorption from aqueous media through the nanotechnology: a review. *J. Mater. Res. Technol.* **14**, 2195–2218 (2021).

107. Rakshit, R. et al. Influence of functional group of dye on the adsorption behaviour of CoFe 2 O 4 nano-hollow spheres. *New J. Chem.* **41**(17), 9095–9102 (2017).

108. Shoaib, A. G., Ragab, S., El Sikaily, A., Yılmaz, M. & Nemr, E. A. Thermodynamic, kinetic, and isotherm studies of Direct Blue 86 dye absorption by cellulose hydrogel. *Sci. Rep.* **13**(1), 5910 (2023).

109. Castellar-Ortega, G. et al. Equilibrium, kinetic and thermodynamic of direct blue 86 dye adsorption on activated carbon obtained from manioc husk. *Rev. MVZ Córdoba* **24**(2), 7231–7238 (2019).

110. Garg, D., Majumder, C. B., Kumar, S. & Sarkar, B. Removal of Direct Blue-86 dye from aqueous solution using alginate encapsulated activated carbon (PnsAC-alginate) prepared from waste peanut shell. *J. Environ. Chem. Eng.* **7**(5), 103365 (2019).

111. El Sikaily, A., El Nemr, A., Khaled, A. & Abdelwahab, O. Removal of toxic chromium from wastewater using green alga Ulva lactuca and its activated Carbon. *J. Hazard. Mater.* **148**, 216–228 (2007).

112. El-Nemr, M. A., Abdelmonem, N. M., Ismail, I. M., Ragab, S. & El Nemr, A. Ozone and ammonium hydroxide modification of biochar prepared from *Pisum sativum* peels improves the adsorption of copper (II) from an aqueous medium. *Environ. Process.* **7**, 973–1007 (2020).

113. El Nemr, A. Potential of pomegranate husk carbon for cr(VI) removal from wastewater: kinetic and isotherm studies. *J. Hazard. Mater.* **161**, 132–141 (2009).

114. Eleryan, A. et al. Mandarin Biochar-TETA (MBT) prepared from Citrus reticulata peels for adsorption of Acid Yellow 11 dye from water. *Sci. Rep.* **12**, 7859. https://doi.org/10.1038/s41598-022-22359-x (2022).

115. El Nemr, A., Abdelwahab, O., Khaled, A. & El Sikaily, A. Removal of direct blue-86 from aqueous solution by new activated carbon developed from orange peel. *J. Hazard. Mater.* **161**, 102–110 (2009).
116. Parshetti, G. K., Hoekman, S. K. & Balasubramanian, R. Chemical, structural and combustion characteristics of carbonaceous products obtained by hydrothermal carbonization of palm empty fruit bunches. *Bioresour. Technol.* **135**, 683–689 (2013).
117. Tsai, W. T. & Chen, H. R. Adsorption kinetics of herbicide paraquat in aqueous solution onto a low-cost adsorbent, swine-manure-derived biochar. *Int. J. Environ. Sci. Technol.* **10**, 1349–1356 (2013).
118. Xu, R. K., Xiao, S. C., Yuan, J. H. & Zhao, A. Z. Adsorption of methyl violet from aqueous solutions by the biochars derived from crop residues. *Bioresour. Technol.* **102**, 10293–10298. https://doi.org/10.1016/j.biortech.2011.08.089 (2011).
119. Hassaan, M. A. et al. Advanced oxidation of acid yellow 11 dye; detoxification and degradation mechanism. *Toxin Rev.* **40**(4), 1472–1480. https://doi.org/10.1080/15569543.2020.1736098 (2021).
120. El-Nemr, M. A. et al. Isotherm and kinetic studies of acid yellow 11 dye adsorption from wastewater using Pisum Sativum peels microporous activated carbon. *Sci. Rep.* **13**(1), 4268. https://doi.org/10.1038/s41598-023-31433-x (2023).
121. Ali, R. M. et al. Towards potential removal of malachite green from wastewater: adsorption process optimization and prediction. In *Materials Science Forum, vol. 1008* 213–221 (Trans Tech Publications Ltd.. 2020).
122. El-Nemr, M. A. et al. Adsorption of Cr^{6+} ion using activated Pisum sativum peels-triethylenetetramine. *Environ. Sci. Pollut. Res.* **29**(60), 91036–91060. https://doi.org/10.1007/s11356-022-21957-6 (2022).
123. Rajumon, R. et al. Adsorption of textile dyes with ultrasonic assistance using green reduced graphene oxide: an in-depth investigation on sonochemical factors. *J. Environ. Chem. Engi.* **7**(6), 103479 (2019).
124. Ealias, A. M. & Saravanakumar, M. P. Facile synthesis and characterisation of AlNs using protein Rich Solution extracted from sewage sludge and its application for ultrasonic assisted dye adsorption: isotherms, kinetics, mechanism and RSM design. *J. Environ. Manage.* **206**, 215–227 (2018).
125. Aragaw, T. A. & Bogale, F. M. Biomass-based adsorbents for removal of dyes from wastewater: a review. *Front. Environ. Sci.* **9**, 1–24. https://doi.org/10.3389/fenvs.2021.764958 (2021).

Author contributions

Dr. A. Eleryan and Dr. M.A. Hassaan conducted the experiment, calculation and theoretical models. Dr. M.A. Hassaan carried out the characterization, Dr. S. Ragab read the manuscript and supervised the experimental work, and Dr. U.O. Aigbe, Dr. K.E. Ukhurebor, Dr. O.A. Osibote and Dr. I. Hossain wrote the original manuscript. Prof. A. El Nemr supervised the experimental work, completed the manuscript and provided financial support for the experiment work.

Funding

Competing interests

The authors declare no competing interests.

Additional information

Supplementary Information The online version contains supplementary material available at https://doi.org/10.1038/s41598-025-85405-4.

Correspondence and requests for materials should be addressed to A.E.N.

Reprints and permissions information is available at www.nature.com/reprints.

Publisher's note Springer Nature remains neutral with regard to jurisdictional claims in published maps and institutional affiliations.